LITHIUM NIOBATE MEMS DEVICE BY PICOSECOND LASER MACHINING

LITHIUM NIOBATE MEMS DEVICE BY PICOSECOND LASER MACHINING

By

YUAN HE, M.ENG.

A Thesis
Submitted to the School of Graduate Studies
in Partial Fulfilment of the Requirements
for the Degree
Master of Applied Science

McMaster University

MASTER OF APPLIED SCIENCE (2008) McMaster University
(Engineering Physics) Hamilton, Ontario

TITLE: Lithium Niobate MEMS Device by Picosecond Laser Machining

AUTHOR: Yuan He, M.Eng. (Shandong University)

SUPERVISORS: Dr. Rafael N. Kleiman and Dr. John S. Preston

NUMBER OF PAGES: 66

Abstract

Lithium niobate has interesting characteristics such as the electro-optic effect, the acousto-optic effect, piezoelectricity and large nonlinear optical coefficients. Potential applications in MEMS field could be explored if microstructures are fabricated in lithium niobate substrates,. This thesis presents the fabrication and characterization of a lithium niobate MEMS device. As lithium niobate crystal is difficult to process using standard semiconductor techniques including both wet etching and dry etching, new methods are required to process lithium niobate. In our project, picosecond laser pulses were chosen to produce bridges on lithium niobate. Fabrication of grooves with high aspect ratio were attempted and grooves with clean morphology were obtained when laser pulses with low cutting speed, medium pulse energy, and large number of passes were employed. This shows picosecond laser machining is a viable method to process lithium niobate.

Waveguides in Z cut lithium niobate crystal were fabricated using Ti-indiffusion techniques. After the fabrication of waveguides in lithium niobate, a SiO_2 film with a thickness of 0.3μm was deposited as a buffer layer. Ti-Pt-Au electrodes for actuation function were then deposited through lift-off technique. Finally a bridge structure (80um in width and 600um in length) with a waveguide embedded in it was fabricated with picosecond laser. The insertion loss before and after laser machining was 6.99dB and 5.01dB respectively.

Optical and electrical tests were performed in an effort to determine the resonance frequency of bridge. In the optical test, many bulk piezoelectric resonance peaks were presented in the frequency spectrum. After damping the vibration of substrate, these spikes disappeared and only a background noise with small spikes were obtained. As those small spikes are not reproducible, the optical test is not a viable method to

determine resonance frequency of the bridge structure in our device. The electrical test was then carried out in a vacuum environment in order to find the resonance frequency. The spectrum presents a spike with large amplitude. However, the phase and amplitude of the spike remained the same when the vacuum condition was removed, which indicates the spike is not related to the resonance of the bridge. In summary, the resonance frequency of bridge structure could not be determined by these two approaches.

Future work could involve directly investigating the material properties surrounding the machining region to see whether the piezoelectricity of the material has been damaged from laser ablation process. New laser machining process of lithium niobate may also need to be studied to avoid this damage to the substrate structure. Even though our device could not be driven to vibrate at its resonance frequency, it is worth making microstructures in lithium niobate substrates. The combination of optical, mechanical and electrical elements will make lithium niobate a great potential material for optical MEMS applications.

Acknowledgements

Without the help of many people from Engineering Physics Department throughout my graduate studies, the work contained in this project would not have been possible. My supervisors, Rafael Kleiman and John Preston have offered a vast amount of guidance and assistance. I will be happy if I can have a chance of working with them in the future. I am grateful to Dr. Changqing Xu and Dr. Wanguo Liang for their generous help with the fabrication processes of our device. When I stayed in the femtosecond laser lab, Dr. Harold Haugen, Henry Tiedje, Travis Crawford, Hsu Eugene provided continuous assistance for my research. Dr. Zhling Peng was always there when I needed help and he trained me on fabrication processes. Doris Stevanovic, Bruce Doug and Graham Pearson were offering help with my project all the time. I also would like to thank the students in my group, Edgar Huante, Zdanovich Andrey, Ruchi Gupta, and Rampal Abhishaik for giving me the two years of enjoyable memories in my life. Finally, I would like to thank my family for their love, patience and support.

Table of Contents

List of Figures

Chapter 1 Overview

1.1 Introduction

Lithium niobate ($LiNbO_3$) is a material of considerable interest for integrated and waveguide optics. In crystalline form, Lithium niobate has many attractive characteristics such as the electro-optic effect, the acousto-optic effect, piezoelectricity and large nonlinear optical coefficients. Because of these properties and the availability of high quality, large size wafers grown by the Czochralski method, lithium niobate has been widely used in optical communications and sensor systems. Optical modulators, directional couplers, surface acoustic wave devices and nonlinear optics devices with periodically poled structures have been fabricated on lithium niobate crystals [1].

Micro-Opto-Electromechanical Systems (MOEMS) is the integration of optical, mechanical and electronic elements on a substrate (usually silicon) through modern microfabrication technologies for applications in sensors and actuators. Most MOEMS devices are based on silicon technologies due to the maturity of semiconductor fabrication processes and low cost of silicon wafers. Among all the actuation approaches, electrostatic actuation is the most popular technique for silicon-based MOEMS. However, it has the limitation of the $1/r^2$ dependence between applied force and distance according to Coulomb's Law, while using lithium niobate provides the possibility of using converse piezoelectric actuation in which the extension is directly proportional to the voltage. Also, the energy density in some ferroelectric materials like PZT is ten times greater than with electrostatics, and this may give the potential for lower actuation voltage and faster switching speed. Finally, there is an opportunity to couple the optical, electrical and mechanical domains in one device. Therefore, Lithium Niobate could be a good substrate candidate for MOEMS applications considering the above as well as its excellent mechanical and optical properties.

One well-known application of lithium niobate in MEMS field is surface acoustic waves (SAW) devices, which combine acousto-optic effect and piezoelectric effect to control the incident light beam. Other applications include high-speed optical modulators used in optical communication systems and nonlinear optical frequency-conversion systems.

Unfortunately, standard semiconductor processing techniques including both wet etching [2] and dry etching [3] are well known to be difficult on $LiNbO_3$. An alternative approach is to utilize ultrafast-pulsed laser to ablate lithium niobate in order to produce microstructures on it [4]. Paul Driedger [5] has investigated the femotosecond laser machining of lithium niobate. As shown in his thesis, machining of craters, grooves and cantilevers is possible. He also noted that different behaviors due to the complex material structure have been found under different laser conditions. By using femtosecond laser with multiple passes and laser polarization perpendicular to the grooves in the ablation regime, deep grooves with high aspect ratio were achieved. However, the influence of laser machining conditions on the optical and mechanical properties of substrates has not been investigated.

This thesis first presents an investigation of the laser parameters for machining bridge and cantilever structures with the required feature sizes in lithium niobate. Although Paul Driedger's work suggested using high cutting speed associated with high laser powers as it gives a clean machining morphology and helps the machining stay in the ablation region, it was found out that increased variation of groove depth was related to the high laser cutting speed. More importantly, the waveguide showed smaller insertion loss when a low cutting speed was used to make the bridge.

In the test devices, electrodes are deposited on top of the substrate for the actuation of the device before machining the bridge structure in lithium niobate. The insertion loss of the device was characterized and resonant frequency of the bridge was investigated.

Optical and electrical tests were performed in an effort to determine the resonance frequency. An optical waveguide with two polished endfaces can be regarded as a Fabry-Perot resonant cavity. Light propagates through the waveguide and reflects at both facets. The amount of reflection is determined by the refractive indices of the waveguide and the external media. As the waves pass the waveguide path back and forth, a standing wave is produced which makes the output of the waveguide sensitive to the effective length of the cavity. When the waveguide is built into a bridge and the bridge experiences a vibration at resonance frequency, then phase shift reaches the maximum and thus the optical intensity of the transmitted light undergoes the biggest change. The electrical test is to investigate the resulting current in response to the application of external voltage signal from a function generator.

However, we did not find the resonance frequency of the fabricated bridge in both tests. In the optical test, many bulk material piezoelectric resonance were presented in the frequency spectrum. After fixing the sample to a glass slide to damp the vibration of the substrate, these spikes disappeared and only a background noise with small spikes were shown in the spectrum. Through experiments it was found that the spectrum results are not reproducible, and therefore the optical test is not a viable method to determine resonance frequency of the bridge structure in our device.

The electrical test was carried out in a vacuum environment. A spike with large amplitude was found. After removing the vacuum condition, the phase and amplitude of the spike remained the same. This indicates the spike is not affected by the vacuum condition and thus is not related to the resonance of the bridge.

Although the device could not be driven to vibrate at its resonance frequency, it is still worth fabricating microstructures in lithium niobate substrate considering the great potential of lithium niobate crystal in MEMS applications. Future work could be investigating the properties of material surrounding the machining area to examine if the piezoelectricity of bridge structure has been damaged from laser machining.

Chapter 2 introduces general properties of lithium niobate and some effects related to the actuation mechanism of our device. Chapter 3 discusses the ultrafast laser machining of material, the machining operating system and machining procedures. This is followed by a review of the results of laser machining of $LiNbO_3$ by Paul Driedger. Chapter 4 presents the investigation of laser machining results as a function of some key laser parameters. Chapter 5 presents the design and fabrication of $LiNbO_3$ device. In Chapter 6, the optical properties of the device are characterized and resonant frequency of the bridge is investigated through optical and electrical tests.

Chapter 2 Fundamentals of Lithium Niobate

This chapter presents the basic concepts that are related to driving mechanism of the $LiNbO_3$ MEMS device fabricated in this project. These include the piezoelectric effect, the electro-optic effect and the photoelastic effect. These descriptions will provide a good understanding of the operating principals and performance of the device described in this thesis.

2.1 Basic Properties of Lithium Niobate

Lithium niobate crystal structure belongs to the trigonal 3m point group. It is negative optical unaxial with two refractive indices n_o and n_e. Pure lithium niobate crystal is transparent from 350nm (corresponding to the bandgap of 3.75eV) to the first infrared vibration absorption at around 5μm (~0.25eV), which ensures a wide spectral window for photonic applications.

Crystal symmetry	Trigonal, point group 3m
Single crystal growth method	Czochralski method
transparency region	0.35 μm ~5 μm
Curie temperature	T=1150 °C
optical anisotropy	uniaxial, c-axis
refractive indices (at 632.8 nm)	$n_o = 2.286$, $n_e = 2.203$
optical effects	acousto-optic effect electro-optic effect second order nonlinear effect piezoelectric effect photorefractive effect

Table 2-1 Main properties of $LiNbO_3$ crystal

Lithium niobate is ferroelectric below its Curie temperature (~1150°C). An unpoled $LiNbO_3$ crystal consists of domain regions where directions of polarization are parallel but in opposite direction. The presence of domains can affect some of the macroscopic properties (e.g. piezoelectricity) of crystal but not the others like refractive index. In our experiments, commercially sold $LiNbO_3$ wafers are utilized and they are single domain crystal.

The Czochralski crystal growth method is used to grow lithium niobate with consistent quality (optical homogeneity of commercial crystal: $\Delta n \sim 10^{-5}$). From these inexpensive wafers with excellent optical properties can be easily fabricated. The main properties of lithium niobate crystal are summarized in Table I.

2.2 Piezoelectric Effect

Piezoelectricity was discovered by the brothers Curie in 1880. Through a series of experiments, the brother verified that provided materials had the correct underlying microscopic structure, macroscopic electric surface charges were produced when mechanical stress was applied to the materials. Examples of piezoelectric materials include quartz and zincblende. This phenomenon was later named as piezoelectric effect. Nowadays piezoelectric devices are widely used for transducers for applications including telephone speakers and sonar arrays.

Piezoelectricity is an interaction between the electrical and mechanical response of a material. A piezoelectric crystal is defined as a crystal in which an electric polarization is produced in response to applied stress. The phenomena can be understood in a simple way. Many crystals consist of several positive and negative ions that usually neutralize one another and thus there is no dipole moment. When stress is applied to the crystal, it undergoes deformation and causes a resultant positive charge on one face of the crystal, and a resultant negative charge on the other face. A clear requirement for piezoelectricity is that the material does not have a centre of inversion symmetry.

Piezoelectricity is reversible, which means strain is created when applying an electric field to the crystal. The converse effect can be predicted from thermodynamic point of view. The converse piezoelectric effect, for which an applied field causes a resultant strain, is one of the popular actuation methods for MEMS devices. These two effects only occur to some special classes of crystals that have polar axes, and opposite charges are developed at the two ends of polar axes. All crystals that are ferroelectric materials also exhibit piezoelectric effect. However, a crystal could be piezoelectric without being ferroelectric.

The nature of charges developed on the surfaces of the crystal depends on the applied stress – a reversal of the nature of stress reverses the nature of the accumulated charges developed on the surfaces. In a similar way, if a positive electric field generates an elongation strain in a piezoelectric material, then the reversal of the electric field produce a compressional strain. The produced strain is linearly proportional to the applied electric field.

The strains produced depend on the product of the piezoelectric tensor coefficient and the component of applied electric field. Piezoelectricity couples the mechanical strain field S (second-rank tensor) with the electric field E (tensor of rank one), and therefore piezoelectricity is a third-rank tensor property. d is (3×6) piezoelectric matrices (m/V). The mechanical strain field is given by Equation 2-1.

$$\begin{bmatrix} S_1 \\ S_2 \\ S_3 \\ S_4 \\ S_5 \\ S_6 \end{bmatrix} = \begin{bmatrix} 0 & -d_{22} & d_{31} \\ 0 & d_{22} & d_{31} \\ 0 & 0 & d_{33} \\ 0 & d_{15} & 0 \\ d_{15} & 0 & 0 \\ -d_{22} & 0 & 0 \end{bmatrix} \begin{bmatrix} E_1 \\ E_2 \\ E_3 \end{bmatrix} = \begin{bmatrix} -d_{22}E_2 + d_{31}E_3 \\ d_{22}E_2 + d_{31}E_3 \\ d_{33}E_3 \\ d_{15}E_2 \\ d_{15}E_1 \\ -d_{22}E_1 \end{bmatrix} \qquad \textbf{2-1}$$

2.3 Electro-optic Effect

By electro-optical effect, we mean the phenomenon of the change in the refractive indices of the crystal due to apply of electrical field. The shape, the size and the orientation of optical indicatrix may be changed.

The refractive index n as a function of applied electrical field E can be described as in Equation 2-2:

$$n(E) = n + \alpha_1 E + \frac{1}{2}\alpha_2 E^2 + \cdots \qquad \textbf{2-2}$$

The Pockels effect is associated with α_1 and only exists in non-centrosymmetric materials and is material dependent. In materials that exhibit the Pockels effect, this linear effect is usually much larger than the Kerr effect associated with α_2. Like photoelastic effect, electro-optic birefringence is linearly proportional to the applied electric field. Under the action of an electric field, the optical properties of crystal changes. The optical properties of crystal can be represented by an optical index ellipsoid, which can be described by the Equation 2-3:

$$\frac{x^2}{n_x^2} + \frac{y^2}{n_y^2} + \frac{z^2}{n_z^2} = 1 \qquad \textbf{2-3}$$

where n_x, n_y, n_z are the refractive indices along the principal axes.

There is a second way to describe the index ellipsoid. The impermittivity tensor, β is the reciprocal of dielectric tensor and can be defined as $\beta_{ij} = \varepsilon^{-1}$, where ε is the permittivity tensor. Thus the relative impermittivity B can be described by $B = \varepsilon_0 \beta$.

In the principal axis system, B is given by Equation 2-4:

$$B = \begin{bmatrix} \frac{1}{n_x^2} & 0 & 0 \\ 0 & \frac{1}{n_y^2} & 0 \\ 0 & 0 & \frac{1}{n_z^2} \end{bmatrix} \qquad \textbf{2-4}$$

The index ellipsoid can then be given by Equation 2-5:

$$\sum_{i,j=1}^{3} B_{ij} x_i x_j = 1 \qquad \textbf{2-5}$$

The Pockels effect can be expressed by the impermeability tensor:

$$\Delta B_{ij} = r_{ijk} E_k \qquad \textbf{2-6}$$

,where r_{ijk} is the third-rank tensor of electro-optic coefficient.

As ΔB_{ij} is symmetric, according to the substitution rule:

$$\begin{aligned} & jk = 11 \to 1, jk = 22 \to 2 \\ & jk = 33 \to 3, jk = 23,32 \to 4 \\ & jk = 31,13 \to 5, jk = 12,21 \to 6 \end{aligned} \qquad \textbf{2-7}$$

We can then simplify Equation 2-6 to be:

$$\Delta B_i = r_{ij} E_j (i = 1,2,...6; j = 1,2,3) \qquad \textbf{2-8}$$

Therefore the index ellipsoid is given by:

$$(\frac{1}{n^2})_1 x^2 + (\frac{1}{n^2})_2 y^2 + (\frac{1}{n^2})_3 z^2 + 2(\frac{1}{n^2})_4 yz + 2(\frac{1}{n^2})_5 zx + 2(\frac{1}{n^2})_6 xy = 1 \qquad \textbf{2-9}$$

Some matrix elements of r_{ij} will be constrained to zero or pairs of elements maybe constrained to be the same or opposites due to the crystal classes.

Lithium niobate is negative uniaxial crystal belonging to 3m crystal group. Therefore Equation 2-8 can be written as:

$$\begin{bmatrix} \frac{1}{n_1^2} \\ \frac{1}{n_2^2} \\ \frac{1}{n_3^2} \\ \frac{1}{n_4^2} \\ \frac{1}{n_5^2} \\ \frac{1}{n_6^2} \end{bmatrix} = \begin{bmatrix} 0 & -r_{22} & r_{13} \\ 0 & r_{22} & r_{13} \\ 0 & 0 & r_{33} \\ 0 & r_{51} & 0 \\ r_{51} & 0 & 0 \\ -r_{22} & 0 & 0 \end{bmatrix} \begin{bmatrix} E_1 \\ E_2 \\ E_3 \end{bmatrix} = \begin{bmatrix} -r_{22}E_2 + r_{13}E_3 \\ r_{22}E_2 + r_{13}E_3 \\ r_{33}E_3 \\ r_{51}E_2 \\ r_{51}E_1 \\ -r_{22}E_1 \end{bmatrix} \qquad \textbf{2-9}$$

If we assume the electrical field is along the Y direction and the wave is propagating along the X direction, then the changes in the indices perpendicular to the propagation direction are:

$$(\frac{1}{n_0^2} - r_{22}E_2)x^2 + (\frac{1}{n_0^2} + r_{22}E_2)y^2 + \frac{1}{n_e^2}z^2 + 2r_{51}E_2 yz = 1 \qquad \textbf{2-10}$$

The Canonical Equation of the indicatrix has the new form:

$$\begin{aligned}&(\frac{1}{n_0^2}+r_{22}E_2+\frac{r_{51}E_2^2}{\frac{1}{n_0^2}-\frac{1}{n_e^2}+r_{22}E_2})y'^2+(\frac{1}{n_0^2}-r_{22}E_2)x'^2\\&+(\frac{1}{n_0^2}-\frac{r_{51}E_2^2}{\frac{1}{n_0^2}-\frac{1}{n_e^2}+r_{22}E_2})z'^2=1\end{aligned} \qquad \textbf{2-11}$$

And the angle by which the principal refractive index ellipsoid will turn about is given by:

$$\tan(2\theta)=\frac{2r_{51}E_2}{\frac{1}{n_0^2}-\frac{1}{n_e^2}+r_{22}E_2} \qquad \textbf{2-12}$$

2.4 Photoelastic Effect

If the density of an optical medium is changed when a stress is applied to it, the refractive index along certain directions will change as a result. In other words, the birefringence generated in a material is directly proportional to the applied stress within the limits of Hooke's law. For example, for an isotropic glass which is stressed along the Z axis (shown in Figure above), the optical path difference ξ can be expressed as: $\xi = v_\lambda P_{zz} T$, where v_λ is called the relative stress-optic coefficient depending on the material, the wavelength of the light used, the nature of stress and the direction of observation. P_{zz} is the stress applied in the Z direction on the face normal to Z axis, and T is the thickness of the sample.

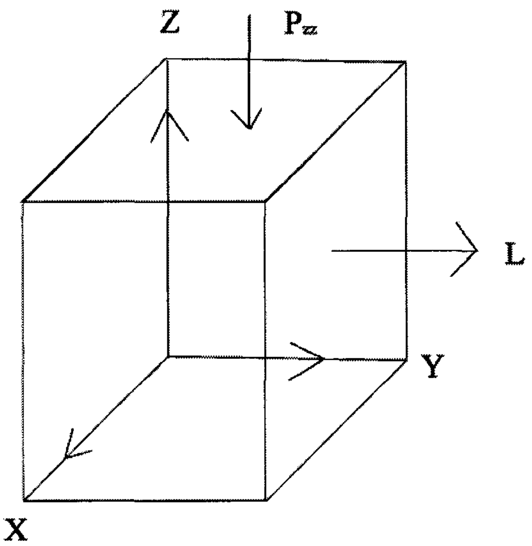

Figure 2-1: An optical material under a linear stress for stress-optical measurements

The photoelastic effect can also described by Pockels' theory, which is also used to illustrate the electro-optic effect. According to Pockels' theory, the photoelastic effect can be described as Equation 2-13:

$$\Delta\left(\frac{1}{n^2}\right)_{ij} = \sum_{k,l} P_{ijkl} S_{kl} \qquad \textbf{2-13}$$

where $\Delta(\frac{1}{n^2})_{ij}$ is the second-rank tensor describing the change in the relative permittivity, S_{kl} is the second-rank tensor describing strain in the crystal, and P_{ijkl} is the fourth-rank strain-optic tensor. The 81 elements of this tensor can be reduced to 36 independent elements and then can be written as a 6×6 matrix in the same way we handle the electro-optic tensor [6]:

$$P_{ijkl} = \begin{bmatrix} p_{11} & p_{12} & p_{13} & p_{14} & 0 & 0 \\ p_{12} & p_{11} & p_{13} & -p_{14} & 0 & 0 \\ p_{31} & p_{31} & p_{33} & 0 & 0 & 0 \\ p_{41} & -p_{41} & 0 & p_{44} & 0 & 0 \\ 0 & 0 & 0 & 0 & p_{44} & p_{41} \\ 0 & 0 & 0 & 0 & p_{14} & (p_{11}-p_{12})/2 \end{bmatrix} \qquad \textbf{2-14}$$

Therefore Equation 2-13 can also be written as:

$$\begin{bmatrix} \frac{1}{n_1^2} \\ \frac{1}{n_2^2} \\ \frac{1}{n_3^2} \\ \frac{1}{n_4^2} \\ \frac{1}{n_5^2} \\ \frac{1}{n_6^2} \end{bmatrix} = \begin{bmatrix} p_{11} & p_{12} & p_{13} & p_{14} & 0 & 0 \\ p_{12} & p_{11} & p_{13} & -p_{14} & 0 & 0 \\ p_{31} & p_{31} & p_{33} & 0 & 0 & 0 \\ p_{41} & -p_{41} & 0 & p_{44} & 0 & 0 \\ 0 & 0 & 0 & 0 & p_{44} & p_{41} \\ 0 & 0 & 0 & 0 & p_{14} & (p_{11}-p_{12})/2 \end{bmatrix} \begin{bmatrix} S_1 \\ S_2 \\ S_3 \\ S_4 \\ S_5 \\ S_6 \end{bmatrix} \qquad \textbf{2-15}$$

2.5 Driving and Testing Mechanism of Device

When applying a voltage to lithium niobate substrates, the electro-optic, piezoelectric, and photoelastic effects are all involved in the operating principle of device. The actual situation may be described by Figure 2-2.

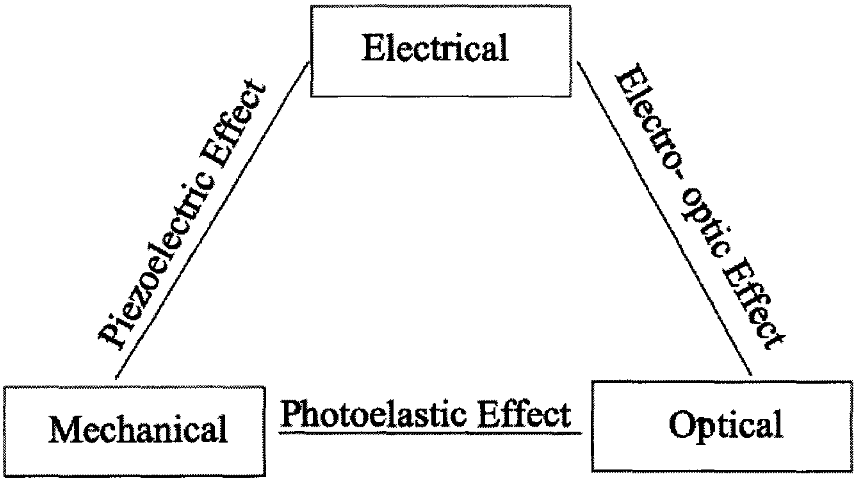

Figure 2-2 Couplings between electrical, mechanical and optical fields

a. Owing to the applied electric field, there is a linear electro-optic effect, which causes a certain amount of optical path difference ϕ_{eo}.

b. Owing to the piezoelectricity of lithium niobate, it experiences a strain when applying an electrical field, causing a photoelastic path difference ϕ_p.

c. In additional to the above two effects, the resultant strain causes the change of the waveguide path length, and therefore leads to an optical path difference ϕ_l.

Thus in total the observed optical path difference ϕ due to the applying of an electrical field to the bridge is given by:

$$\phi = \phi_{eo} + \phi_p + \phi_l$$

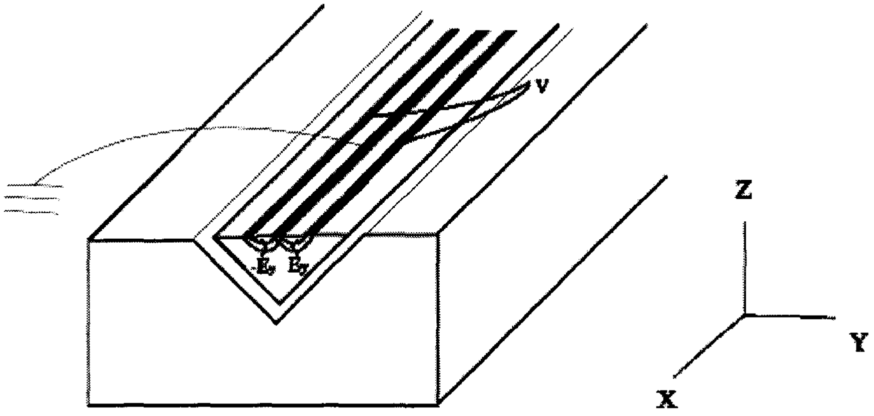

Figure 2-3: Electrodes configuration to drive bridge vibration in Z cut lithium niobate substrate with waveguide along X direction

To utilize the largest converse piezoelectric coefficient d_{22}, we produced a bridge structure with the length along X direction in a Z cut substrate and applied voltage along

Y direction. As can be seen from Figure 2-3, there are three electrodes on top of the bridge. In the normal mode of operation, the central electrode is grounded and voltage, V, is applied to the other two electrodes. In this configuration, the direction of the electrical field is reversed on the two sides of the bridge. This causes one half of the bridge to expand and while the other half is compressed producing a bimorph bridge. The bridge then vibrates at the frequency with which the voltage signal is applied.

Chapter 3 Ultrafast Laser Machining

3.1 Ultrafast Laser Processing

The invention of the ultrafast laser (pulse duration less than 10ps) has provided many new possibilities in the laser-material interactions and processing. With the ultrashort pulse duration, it is simple to achieve high peak laser intensity. For example, a laser with a pulse duration of 150 fs, at a repetition rate of 1000 Hz, and an average output power of 3.5 mW has a peak intensity of 2.4×10^{14} W/cm^2. Due to the short duration of the pulse, the hydrodynamic motion of the material under laser irradiation can be ignored, and no fluid dynamics need to be considered during the pulse.

Long pulsed laser has been extensively used as an efficient machining tool for drilling, cutting and other modification of different materials including metal, dielectrics, and semiconductors. Lasers such as CO_2, Nd:YAG, and excimer lasers are popular for machining because of the noncontact nature of process and environmental concerns. These industrial lasers usually have pulse durations varying from continuous-wave to hundreds of picoseconds.

As to micromachining for subjects with very fine features, at one point excimer lasers were the best choice. They have short wavelength (ultraviolet) and ablate material through a photochemical interaction. However, the potential radiation hazard and the requirement of corrosive gases make them undesirable for certain applications. Nowadays, ultrafast laser in the visible and near infrared region with pulse duration less than 10ps has been well developed owing to the invention of chirped-pulse amplification method. Compared with traditional long pulse laser machining, ultrasfast laser provides additional characteristics such as no wavelength limit for absorption (due to nonlinear absorption), high precision control and the low pulse energies needed.

The laser-material interaction can be explained in a simple way. The electrons are heated by directly absorbing the optical energy. Through collisions with ions the electrons transfer their energy to the ions and hence increase the temperature of the material. The absorbed energy dissipates from the laser focal volume to the area around due to thermal diffusion. For long pulse laser machining, a large volume around the focus point is melted but only a small part reaches the vaporization temperature. For ultrafast laser, the interaction time is much shorter and the laser field strength is much higher. The highly nonequilibrium interaction process involves electrons being driven to much higher temperature than ions and the subsequent thermal diffusion takes places on a much longer time scale than the laser-material interaction time.

In the ultrafast laser-material interaction, the temperature of electrons is lifted to a few tens of electron volts ($1\,ev = 11600\,K$) during the pulse duration, while the ions and lattice temperature is much lower. The electron-ion energy transfer happens mostly after the laser pulse is over, and quickly heats the ions to a high temperature. Most of the material in the interaction volume is vaporized without spending much time in the molten phase. The material is removed by direct vaporizing into air or vacuum (in our case). The material is still heated through heat conduction over a long time scale, but the resultant melt layer is confined to a small volume as the heated material reaches vaporization and the cooling process is rapid due to the steep temperature gradient. Also since most of absorbed energy is carried away during the vaporization, the heat-affected zone is thus much smaller compared to that with a long pulse laser. The heat-affected volume can even be smaller than the focus if the laser fluence is just slightly above the ablation threshold.

At the beginning of laser ablation process, the laser energy is absorbed by the material through either linear or nonlinear absorption. The absorption mechanism varies with the applied laser intensity, pulse duration and target material. For transparent materials like lithium niobate, nonlinear processes (including avalanche ionization and multiphoton ionization) are dominant at the beginning to induce the optical breakdown. After the optical breakdown happens, the transparent material turns into absorbing plasma and the resultant heating of material leads to ablation of the material.

The avalanche ionization process is described in Figure 3-1(a). The transparency characteristic of the material is due to its bandgap being greater than the laser photon energy, so the bound electrons do not absorb the photons at low laser intensity. However, there are always some free or conduction electrons in the material. These so-called “seed electrons” can absorb photons through colliding with the bound electrons and the lattice, in what is called the joule-heating process. When its kinetic energy exceeds the ionization potential of the bound electrons, the collision between the seed electron and bound electron will transfer the energy from the seed electron and another free electron is generated. The repeat of this avalanche process will lead to exponential growth of the electron density. Up to a critical density, a plasma layer forms and the transparent material is broken down into opaque one starting to absorb the energy in a much faster way.

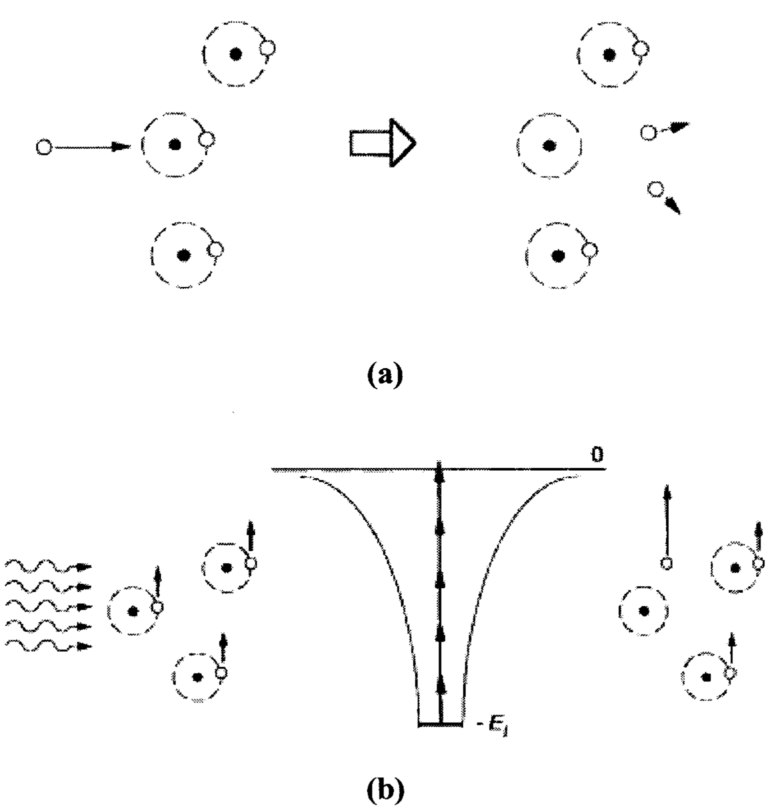

Figure 3-1: (a) Schematic of electron avalanche ionization process, (b) Schematics of multiphoton ionization process [7]

Another nonlinear process that happens in the ultrafast laser-material interaction is multiphoton absorption, which is shown in Figure 3-1(b). During this process, the bound electrons can be directly driven from valence band to conduction band through absorbing n photons provided that $nhv \geq V$, where hv is the photon energy and V is bandgap energy. The multiphoton ionization is only dominant at very high laser field strength. It has been shown that for femotosecond laser machining, the multiphoton ionization supplies the first seed electrons for the breakdown to start, and then avalanche ionization dominates the process.[8]

3.2 Ultrafast Laser Machining of Lithium Niobate

Paul Driedger [5] has studied femotosecond laser ablation of lithium niobate using a commercial 1 kHz amplified Ti: sapphire laser system. He has investigated the dependence of machining morphology on crystal orientation, cutting speed, pulse energy, number of passes and laser polarization.

First, the ablation thresholds for single and multiple consecutive pulses on creating a crater were determined. The ablation threshold is defined as the energy required for ablating the material. Machining of grooves was explored and the dependence of ablation depth on the main laser machining parameters such as cutting speed, fluency and number of consecutive pass were investigated.

Probably due to the complex material structure (a distorted cubic perovskite), the machining results looked more diverse than that of other regular materials like silicon and InP. When creating grooves, two totally different results were found depending on the processing conditions. At low pulse energy and high cutting speed, the machining falls into the ablation regime, where groove with nice morphology (clean edges, little debris and deep depth) were created. At high pulse energy and low cutting speed, the machining transited to modification regime, where shallow grooves were created and the substrate material was modified and became amorphous.

The dependence of groove depth on number of passes was also investigated. At certain cutting speed and energy, the depth increased with the number of passes and then saturated. However, by varying the pulse energy and number of passes, any depth could be obtained. It was found that there was no apparent dependence of ablation depth on crystal orientation and laser polarization. The expectation was that lithium niobate might have shown an anisotropic effect on ablation. The possible reason could be that the incubation distorted the crystal material so that all anisotropic properties were eliminated. The orientation of the laser polarization relative to the cutting direction was found to be relevant and laser polarization perpendicular to the cutting direction was found to give the best groove morphology.

Deep grooves with excellent morphology could be produced by using suitable laser pulse energy and moderate cutting speed with laser polarization perpendicular to the groove. This demonstrates ultrafast laser as a potential tool for creating microstructures such as bridges and cantilevers in lithium niobate.

3.3 Ultrafast Laser Machining Setup and Procedures

The laser utilized for micromachining process was a commercial amplified Ti:Sapphire system (Spectra-Physics Spitfire LCX). The system consists of a Tsunami oscillator, which has a gain medium of Ti:sapphire crystal and a pump source of diode end-pumped Nd:YVO_4 laser at 532nm. Ti: sapphire has been chosen as gain medium for most ultrafast lasers as it has good optical quality and high damage threshold. Theoretically the Ti:sapphire crystals could support femtosecond laser pulses as short as 3fs.

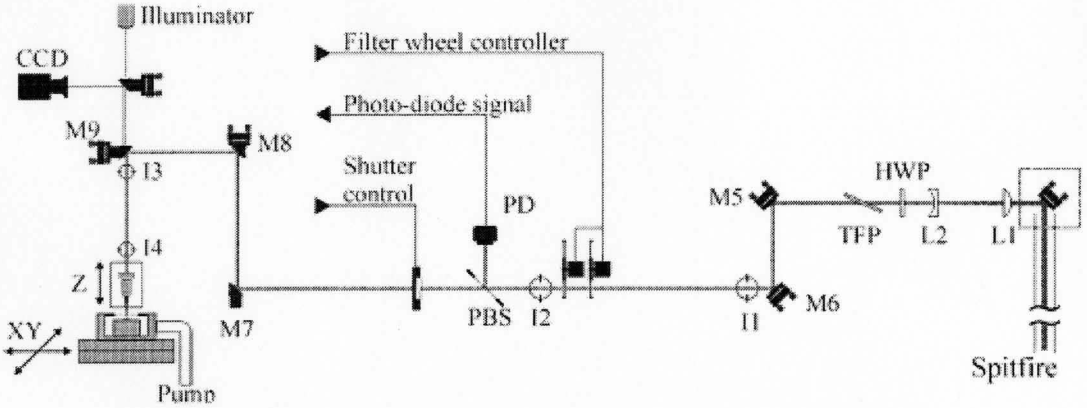

Figure 3-2: Schematic of laser micromachining setup

The laser pulse from Tsunami is amplified when passing through the Spitfire chirped pulse-amplifier (CPA) pumped by the Merlin frequency-doubled Nd:YAG laser. The resultant laser has a linearly polarized pulse with a peak wavelength at 800nm and at a repetition rate of 1000Hz. By tuning the compressor part of the system the pulse duration changes from 150fs to 200ps. This provides us access to the use of both femtosecond and picosecond laser pulses during the laser machining process.

The laser beam from Spitfire is reduced to a diameter about 4mm by a beam condenser consisting of a chromatic doublet (L1, f =50cm) and a plano-concave singlet lens (L2, f = -20cm). Then the pulse energy is typically attenuated to be less than 20 μJ by a combination of a half wave plate (HWP – 0RP44-3, Newport) and a thin film polarizer (TFP – 11BooUP. 26, Newport). In the experiments, the pulse energy can be adjusted by tuning a set of neutral density filters (Model 5294, New Focus). The filters allow simple power adjustments in optical density (OD) steps of 0.1 ($OD=\log(I/I_0)$ where I is the laser intensity).

A fraction of laser power is reflected onto a photodiode by a pellicle beam splitter

(PBS) and the output of photodiode is used to monitor the laser power during the machining. A mechanical shutter (VS25 with VMM-DI controller, Uniblitz) can also be inserted into the optical path to further reduce the repetition of laser pulses. A microscope objective with magnification of 5 × (Mitutoyo M-Plan NIR), a working distance of 4cm and focal length of 3.7cm is usually used to focus the laser onto the sample, which is placed in a vacuumed aluminum chamber through a transparent window. A confocal system and a CCD camera are used to image the machining process on the computer. The position of microscope is adjustable along Z (vertical) direction, and the chamber is mounted on a computer-controlled XYZ translation stage with maximum linear speed of 1000μm/s and the minimum moving step of 0.5μm. Usually the laser pulse has a polarization perpendicular to Y direction.

The spot size ω_0 (spatial radius at of laser beam at $1/e^2$ of peak intensity) and the ablation threshold pulse energy E_{th} can be determined by measuring the craters diameters as a function of pulse energy E and then fitting the data to the well knows Equation 3-1 [9]:

$$D^2 = 2\omega_0^2 \ln(\frac{E}{E_{th}}) \qquad \textbf{3-1}$$

Using the obtained values of E and ω_0 the peak fluence ϕ can be calculated according to the Equation 3-2 [9]:

$$\phi = \frac{2E}{\pi\omega_0^2} \qquad \textbf{3-2}$$

Before the machining process, the output laser needs to be characterized. First the laser spectrum is investigated to make sure the laser has a center wavelength at 800nm and a full-width at half-maximum (FWHM) of 10nm. Then the beam is aligned through alignment irises and a CCD profiler. The next step is to determine the pulse duration by using an intensity autocorrelator. At last, power calibration of OD filters is performed and the data gives a reference for determining the laser power of laser machining during the machining process later.

After the calibration, the sample is placed into the chamber, which is then evacuated to a rough vacuum of 0.1 mbar. A vacuum environment provides machining with the lower ablation threshold and cleaner surface morphology.

The lithium niobate substrates used in the machining process were supplied by Castech Company, China. It is a Z cut crystal with primary flat direction normal to X direction. This is different from the definition of primary flat direction of lithium niobate wafers made in other countries. The wafer is 1mm thick and double side polished. The sample is cleaned by acetone, methanol and deionized water respectively both before and after laser machining.

Chapter 4 Laser machining of Lithium Niobate

Lithium niobate has a wide range of applications in photonics including electro-optic modulators, photorefractive holographic recording and periodically poled lithium niobate crystal for wavelength conversion. With respect to electro-optics lithium niobate is named as "the yardstick against which all other crystals are measured" [10]. Due to its interesting properties, lithium niobate also has potential application in MEMS fields. To make MEMS devices in a lithium niobate substrate, proper methods to create microstructures like bridges and cantilevers are needed. Paul Driedger has demonstrated that fabrication of microstructures in lithium niobate via femotosecond laser ablation is possible[5]. However, his project only presented the results of a preliminary study on femtosecond laser micromachining of lithium niobate. In order to fabricate microstructures with desired feature sizes for MEMS applications, suitable laser parameters should be determined experimentally in order to minimize the laser-produced damage to substrate. Section 4.1 discusses the dependence of laser machining results on laser power, number of passes, magnification of focusing lens and laser pulse duration. Section 4.2 discusses the machining results of free cantilevers and bridges. Finally, a reliable method to produce freestanding structures in lithium niobate substrate by picosecond laser was established.

4.1 Investigation of Laser Machining Results as a Function of Key Laser Parameters

4.11 Groove width versus number of passes and Laser Power

The width of grooves is an important parameter showing how precise the machining process can be and how small the machined feature sized can be achieved. The dependences of groove width on number of passes and laser power were investigated. Z cut sample is used for the experiments. The laser was attenuated by a sequence of neutral density filters with a step of OD=0.1. The spacing between grooves was 100μm. Eight grooves were first produced corresponding to the number of passes of 1, 5, 10, 20, 50, 100, 200 and 500. The power of 3.5mW and cutting speed of 1000μm/s was used here. The second experiment involved the machining of grooves at different laser power corresponding to OD from 0.0 to 1.3.

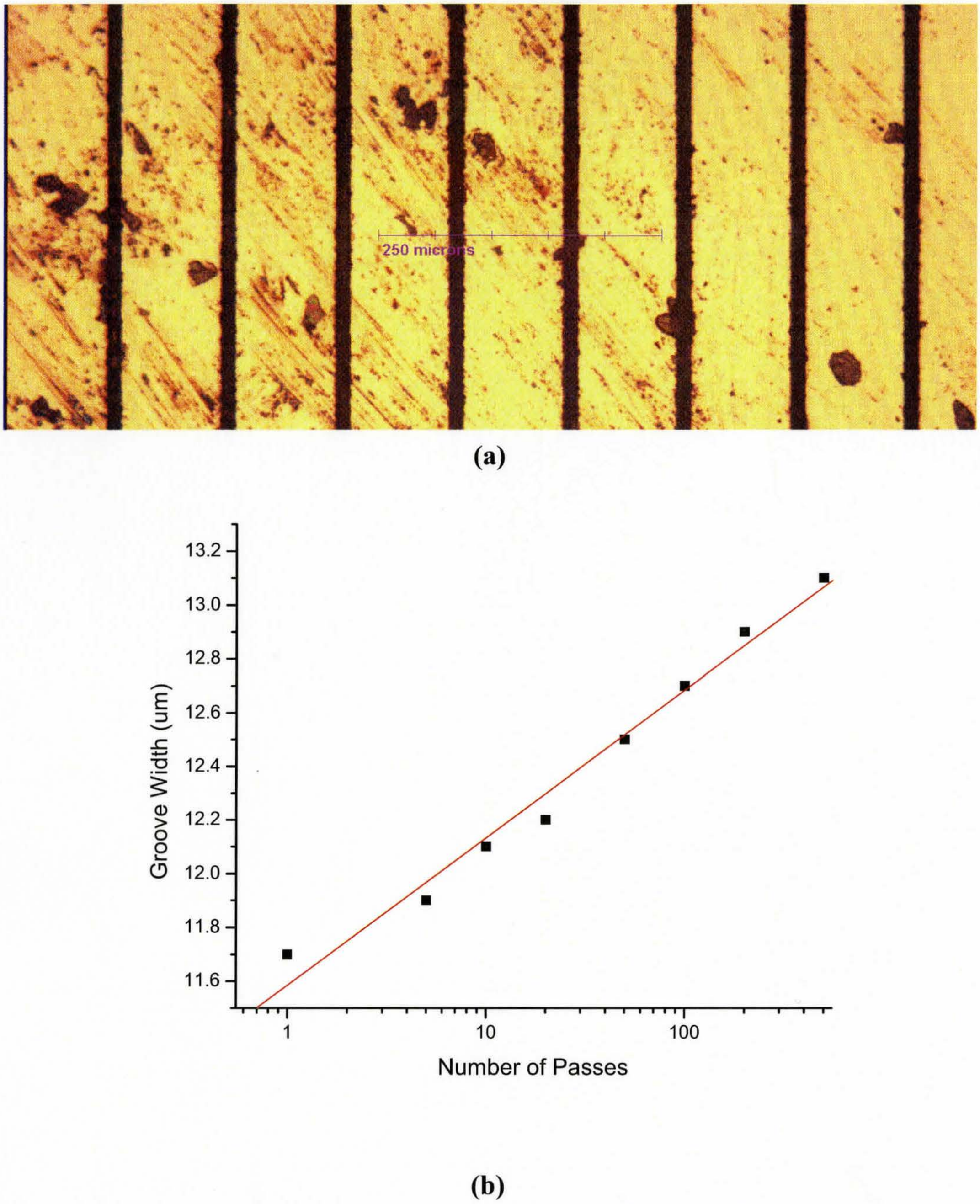

Figure 4-1: (a) Optical image of grooves machined by femtosecond laser at 3.5 mW; number of passes: 1, 5, 10, 20, 50, 100, 200, 500; cutting speed: 1000 µm/s (b) Groove width dependence on number of passes of machining process

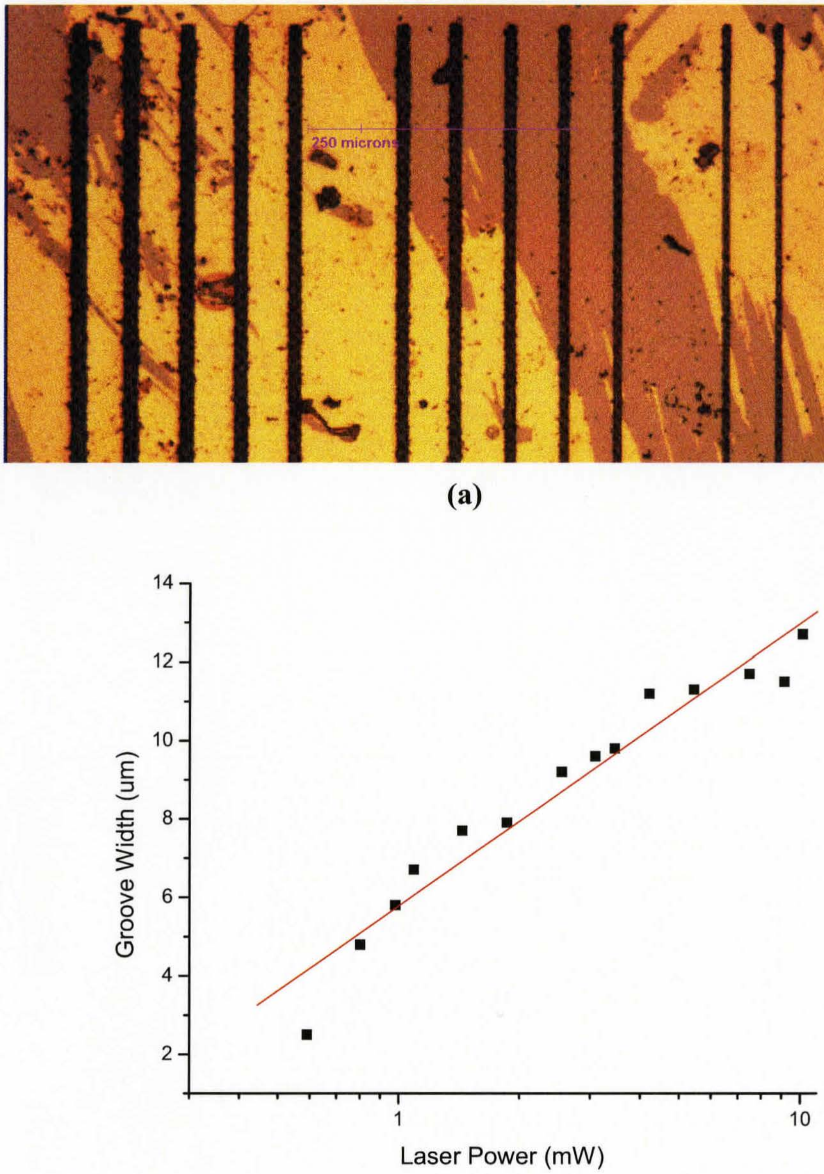

(a)

(b)

Figure 4-2: (a) Optical image of grooves machined by femtosecond laser at single pass with decreased laser power; OD 0.0 - 1.3, OD= 0.0 corresponding to 10mW; cutting speed: 1000 μm/s (b) Groove width dependence on laser power

The width seems to have a logarithmic dependence on the number of passes and laser power. In Figure 4-1 (a), the width increases slowly from 11.7 μm to 13.7 μm with the increase of number of passes from 1 pass to 500 passes. However, as shown in Figure 4-2(a), the width increases considerably from 2.5 μm to 12.7 μm with the increase of laser power from 0.6 mW to 10.1 mW. Figure 4-2 (b) also shows that some parts of grooves are broken when high power was used. These results indicates that, instead of using laser at high power level, a large number of passes are the better choice to create grooves with high aspect ratio.

4.12 Dependence of Groove Depth at Tilted Incidence Cut on Number of Passes and Laser Power

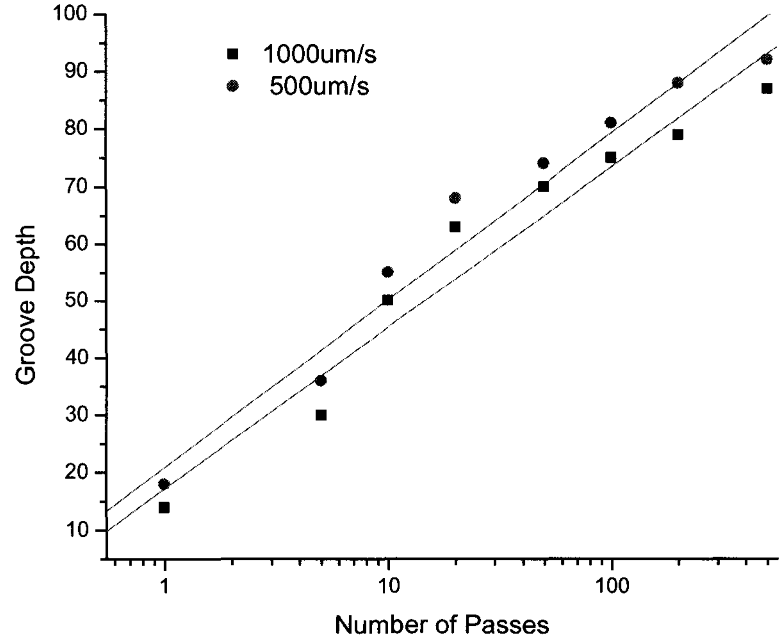

Figure 4-3: Dependence of grooves depth at tilt incidence cut on number of passes with cutting speed of 1000μm/s and laser power of 3.5mW; Groove Length: 750μm; Groove tilt angle relative to horizontal plane: 45°)

Figure 4-3 shows the dependence of grooves depth at tilt incidence cut (Groove tilt angle relative to horizontal plane: 45°) on number of passes with laser power of 3.5mW. The relationship appears to be logarithmic, which is similar to the laser machining results for grooves at normal incidence. A low cutting speed (500μm/s) gives a slight deeper depth and the groove depth cut by 1000μm/s seem to be saturated when the number of passes is more than 100.

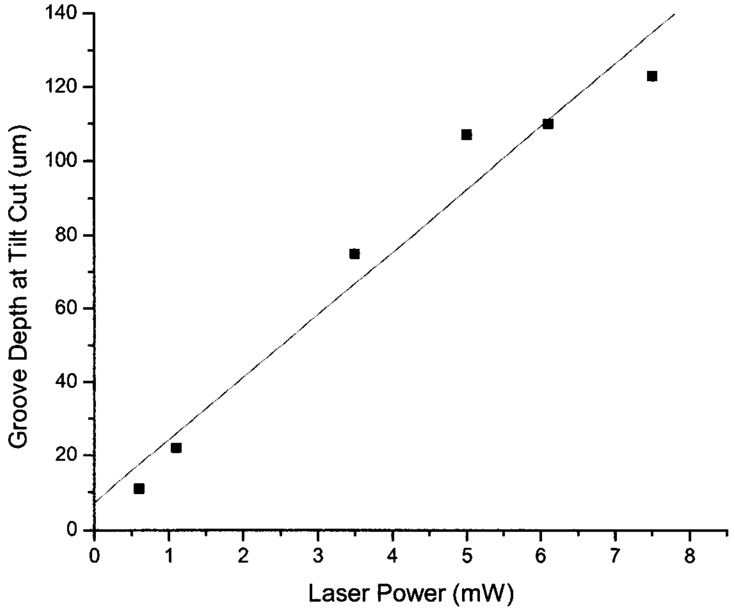

Figure 4-4: Dependence of grooves depth on laser power at tilt incidence cut; Cutting speed: 1000μm/s; Number of passes: 100; Groove Length: 750μm; Groove tilt angle relative to horizontal plane: 45°

In comparison, as shown in Figure 4-4, the depth has a nearly linear relationship with the laser power at constant speed and constant number of passes. Since there is no apparent saturation for the depth of grooves that can be achieved, we may assume any depth is attainable if we apply a sufficient high power laser for machining process. However, one thing to note is the groove width increases considerably with laser power, and it is not favorable to use high laser power to fabricate a structure in lithium niobate if a small feature size is needed.

4.13 Focal Point Location Dependence

During the machining process, it was found out that when focusing the laser beam 40μm below the surface during the laser machining process, deep grooves could be produced (the width only increased slightly). However, if the laser was focused above the surface when machining, shallow grooves with a large width was produced, which is not favorable for producing grooves with high aspect ratio. For producing grooves at tilt incidence, this optimal focal point was found to be around 40μm below the surface, as indicated in Figure 4-5. This indicates when focusing 40μm below the surface the laser intensity on the surface is still higher than the incubation ablation threshold. The value of depth of focus (17μm) for the objective lens utilized make this a reasonable explanation.

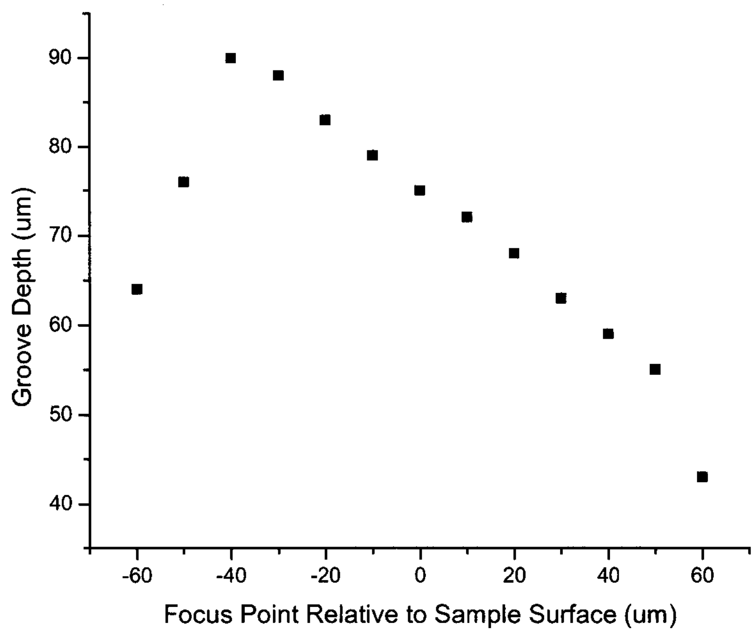

Figure 4-5: Dependence of grooves depth on focal point relative to sample surface; Cutting speed: 1000μm/s, laser power: 3.5mW; number of passes: 100

4.14 Objective lens versus machining results

The laser beam was for most investigations focused on the sample by a 5× microscope objective. Objective lens with a magnification of 10× was also used, and although it did produce much deeper grooves under the same machining conditions there were much more material damage produced. Visible damage occurred around the cutting area even when a low power (~1mW) was used for 10× objective lens to produce grooves, as shown in the middle image of Figure 4-6 (a).

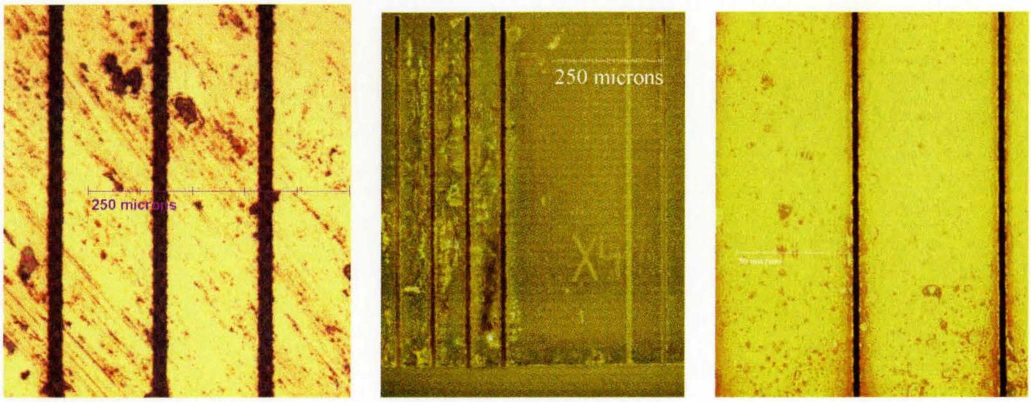

(a)

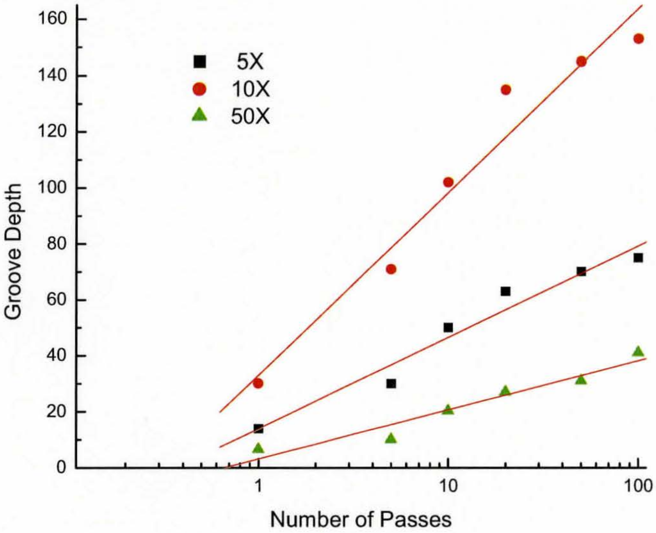

(b)

Figure 4-6: (a) Grooves produced by 5×, 10×, 50× microscope objectives; Laser power: 3.5mW, Cutting speed: 1000μm/s; Number of passes: 100; (b) Dependence of groove depth on number of passes for different objective lens

For 50X lens, grooves with small width (5~11μm) and small depth (6.5~41μm) were achieved with number for passes from 1 to 100. It might be useful to produce cantilevers with small feature size. However, the desired groove depth for creating a bridge with waveguide embedded in it should be around 100μm. In most of our experiments, 5× microscope objective was employed to fabricate bridges.

4.15 Ripples versus Machining Conditions

The depth of a groove produced by laser machining is usually not uniform. For irradiation of stationary object, laser induced periodic surface structures (LIPSS) are well understood [11][12]. These ripples are usually aligned perpendicular to the polarization of the incident laser beam. For a laser beam incident with the polarization perpendicular to the translation direction, the period Λ of the LIPSS is given by [13]:

$$\Lambda = \frac{\lambda}{1 \pm \sin\theta} \qquad \textbf{4-1}$$

where λ is the laser wavelength, and θ is the angle of incidence between the normal and the surface. It is obvious that the LIPSS period is less than the wavelength (~800nm).

The ripples at the bottom of groove in our experiments, however, are not the same phenomenon as LIPSS. The period (~10 μm) is much larger than the typical value for LIPSS and inconsistent with the optical interference responsible for LIPSS. Because of the uncertainty of the groove depth, it is hard to determine the depth of groove by simply measure it at one cross-section of the groove bottom. This difficulty also produces challenges for determining if the fabricated bridge is free from the substrate over its entire length.

There are different ways to observe the groove ripples. For grooves made by tilted cut, by focusing the light on the bottom of the grooves under the transmission mode of optical microscope, ripples with a period of around 10μm and amplitude of a few microns is observed. Figure 4-7 shows the ripples on the bottom for a broken cantilever. The depth of groove also varies at the two ends where the increased depth is due to the deceleration and momentary stopping of the translation stage between passes.

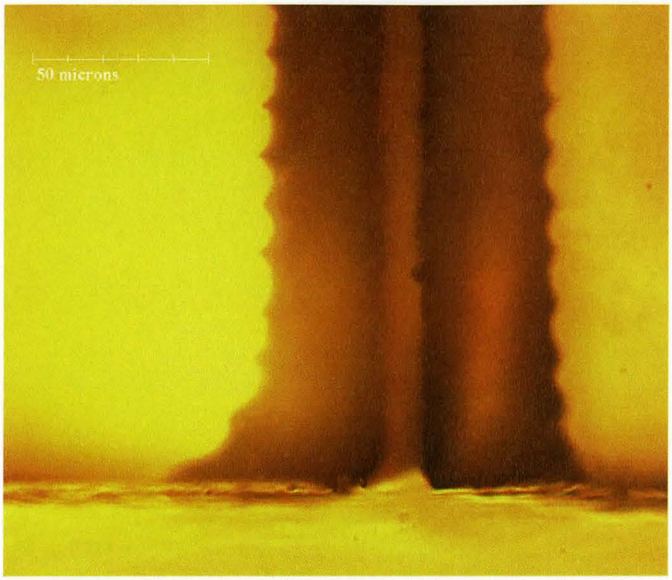

Figure 4-7: Optical image of broken cantilever under transmission mode of optical microscope; Laser power: 3.5mW; Cutting speed: 1000µm/s; Number of passes: 100passes

Another approach is to cut grooves near the side of the sample and then focus onto the groove from the side, as shown in Figure 4-8. The ripples appear to be present for different number of passes. However, the difference in groove depths between the tops and bottoms of the bumps increase with the cutting speed. For example, the amplitude of the bump is very small for grooves made at cutting speeds of 550µm/s or slower, as shown in Figure 4-8.

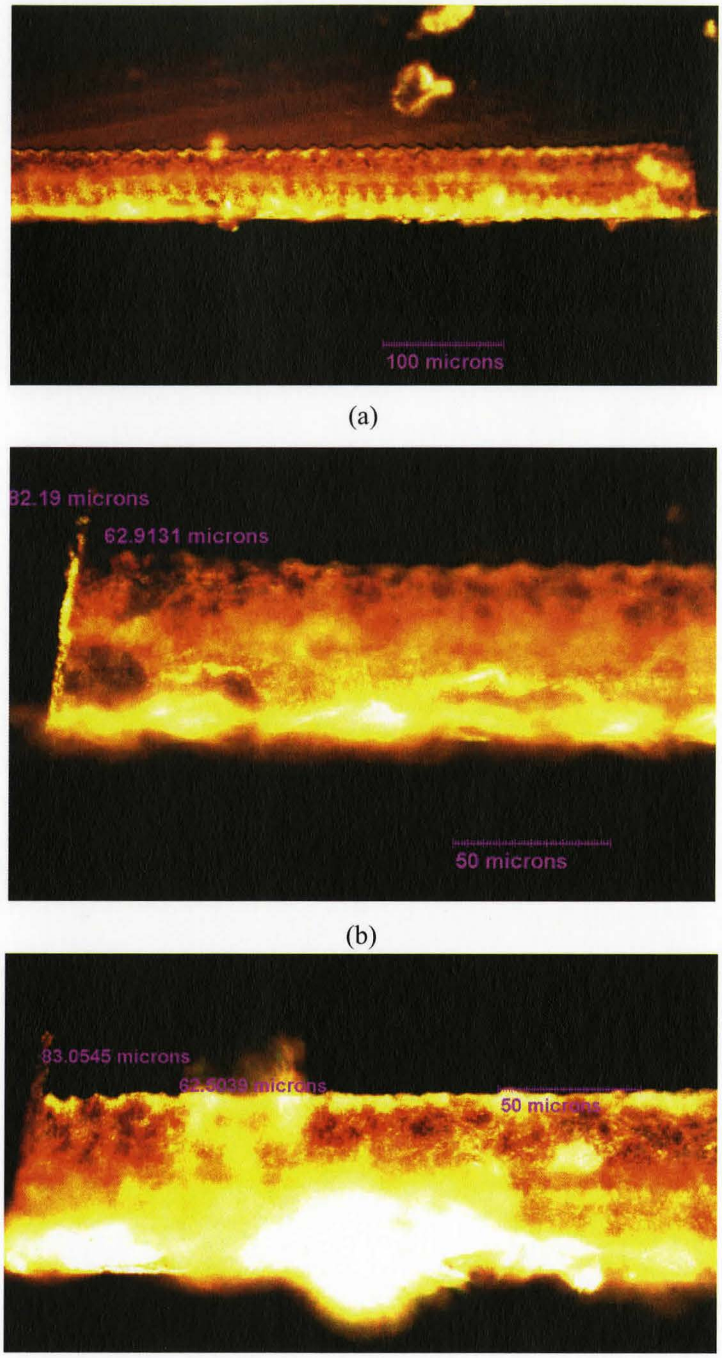

(a)

(b)

(c)

Figure 4-8: Optical image of grooves by laser machining under transmission mode of optical microscope; Laser power: 3.5mW; Cutting speed: 1000μm/s; Number of passes: 100passes (a) 1000μm/s; 20X magnification (b) 1000μm/s; 50X magnification (c) 550μm/s ; 50X magnification

Yet another approach studying the groove profile is to fill the groove with a silicone solution (Sylgard 184 Silicone Elastomer). The ratio of base to curing agent was 10:1. The uncured polymer was poured into the grooves and placed in a vacuum for 25 minutes to force any trapped air out. After this, the polymer was cured at 65 °C for 15.5 hours. Then the polymer was extracted from the groove and studied. Figure 4-9 shows clearly the ripples on the bottom of grooves.

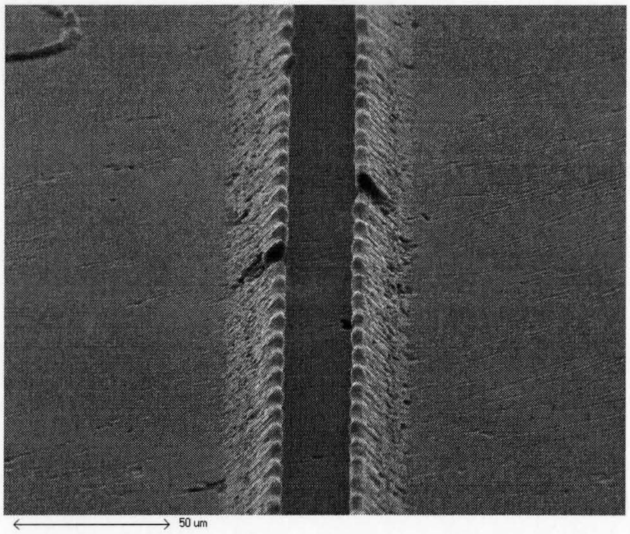

Figure 4-9: Ripples on the bottom of grooves shown by silicone solution

4.16 Femotosecond Laser versus Picosecond Laser Machining

In the machining process, fabrication of triangular cantilevers and bridges were initially attempted using femotosecond laser pulses. However, it was found to be difficult to produce freestanding structures with femotosecond laser pulses, especially for cantilevers. Frequently the structure would be destroyed during the machining or damaged to the point where it was removed by the post-machining cleaning process. Several damaged cantilevers are shown in Figure 4-10. For most of time either part of or all of the structure is gone after the machining or cleaning.

Figure 4-10: Optical images of damaged cantilevers after laser machining

For long laser pulse machining using pulse on the timescale of nanoseconds or longer, the machining process is thermal. The electrons have sufficient time to absorb the incident optical energy and transfer it to the lattice of crystal. Material removal occurs through conventional thermal deposition including melting and boiling of the material. In such a process, a significant amount of heat is transferred to the adjacent material usually leading to a damaged, heat affected zone surrounding the cut area.

By using femtosecond laser pulses for machining process, any material can be machined to micron scale precision with minimal thermal transfer to the remaining material. The process is dominated by plasma formation on a time scale too short for significant energy transfer to the lattice and very limited heat affect zone can be achieved. Due to these advantages, people have been using it widely for applications where micrometer feature sizes are required.

The details of the ablation process depend on a complicated interplay between the material and pulse parameters. Generally it would be expected that for pulse duration less than a few tens of picosecond, laser machining with a picosecond laser pulse has the same mechanism as a femtosecond laser. Figure 4-11 shows that grooves produced by 50 fs laser, 1.0ps and 3.5 ps laser have similar morphologies.

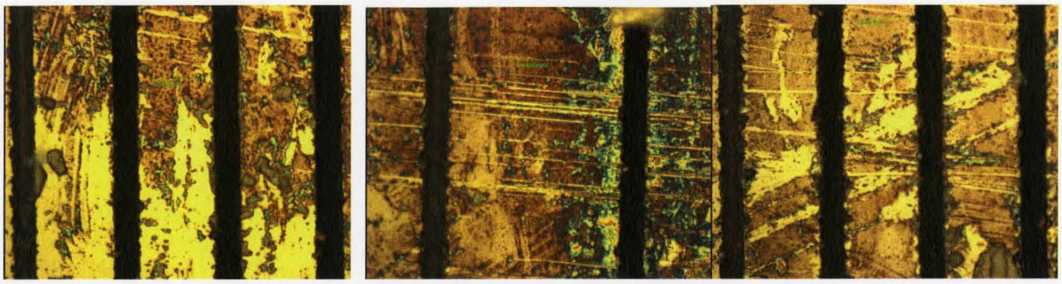

Figure 4-11: Grooves made by 150 fs laser, 1.0ps and 3.5 ps laser (top view)

Also, we found that by using picosecond laser pulses, the fabricated structures are more robust and mechanically stable than those made by femtosecond laser pulses. Figure 4-12 is a comparison of groove depths produced by picosecond laser pulses and femotosecond laser pulse. The depths of fabricated grooves are slightly smaller but this can be compensated if a large number of passes are used.

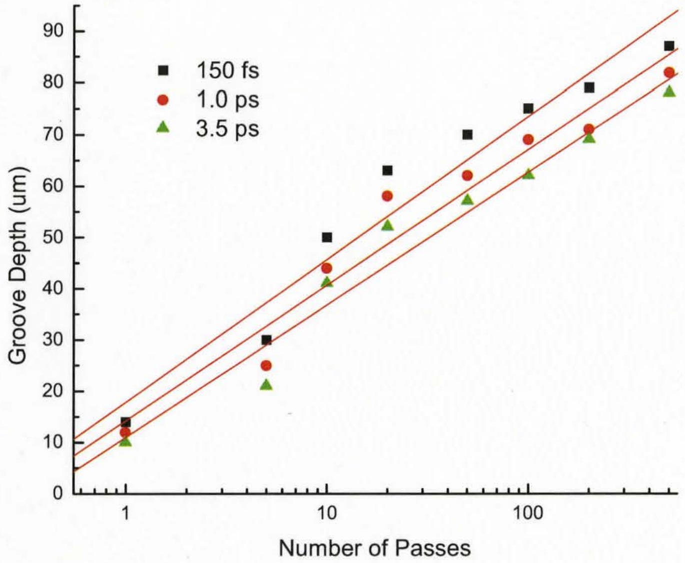

Figure 4-12: Dependence of groove depth on number of passes by laser with different pulse durations

Later in this chapter it will be shown that for optical test of waveguides embedded in fabricated bridges, the optical transmission was higher through waveguides on bridges machined by picosecond pulses. This is consistent with the empirical observation that for this material femotosecond laser pulses create more damage to the surrounded material compared to picosecond laser pulses. These results means picosecond laser is the better choice to produce freestanding microstructures in lithium niobate substrate.

4.2 Producing free cantilevers and bridges

Figure 4-13 shows the top views of grooves with laser machining at normal cut and tilt cut respectively. Both grooves have uniform edges, but the surface color along the grooves is not uniform, which is due to the uneven distribution of the debris. Figure 4-13 (c) shows clearly the periodical color distribution along the groove, which also indicates the depth is not even along the length of groove. Figure 4-10 (d) shows a tilted cut groove image from side view. The groove appears to have smooth surface with a high aspect ratio.

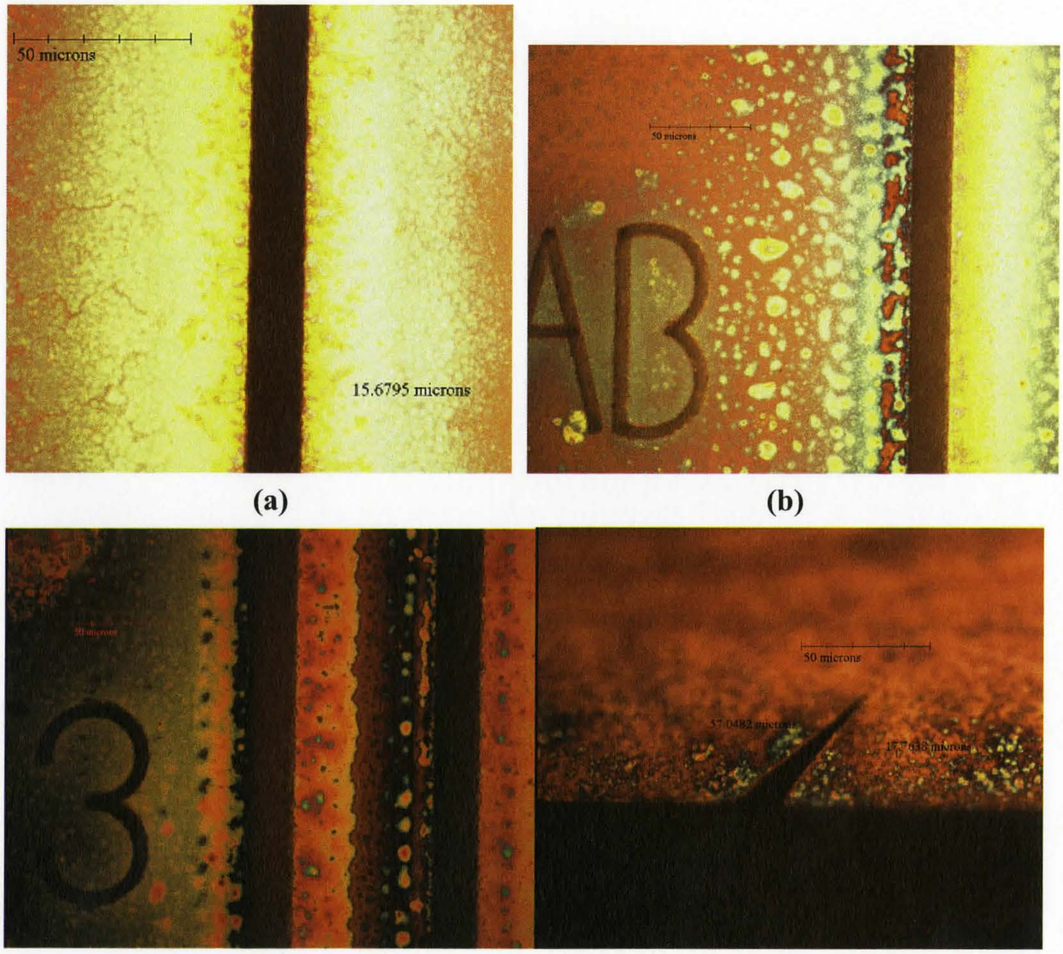

(a) (b)

(c) (d)

Figure 4-13: Optical images of grooves with laser machining at normal cut (a) and tilt cut (b, c, d)

As the end of a cantilever can be observed easily under the optical microscope, we first did the fabrication of cantilevers instead of bridges. Shown in Figure 4-14, there is about 20 μm difference between the two cuts of the cantilever which has been made. Typically the first one had a larger depth.

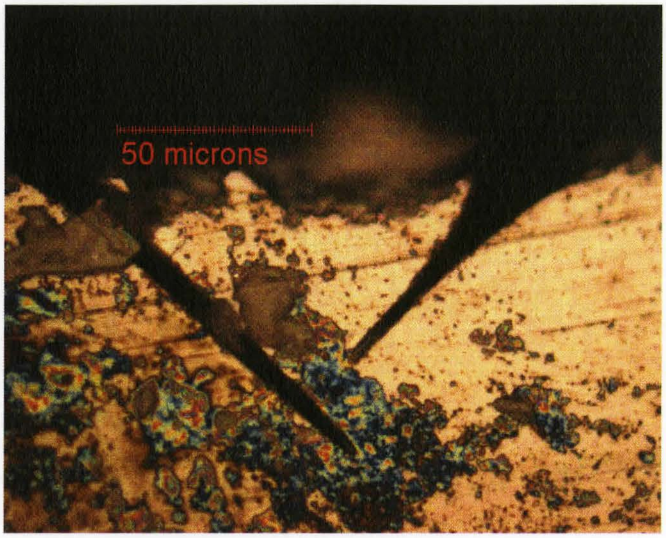

Figure 4-14: Cantilever produced by laser machining without being freestanding; Groove Direction: parallel to Z axis; Polarization: linear and parallel to X axis. Power: 5 mW; Cutting speed: 1000μm/s; Cantilever width: 100μm; Groove Length: 750μm; Number of passes (NOP): 100

Simply looking at the end cross-section is not a reliable method to judge if a cantilever is freestanding because machining process usually yields a much deeper depth at both ends owing to the deceleration of the translation stage. By checking its vertical position relative to the sample surface, we may determine if a cantilever is freestanding. The cantilever is usually raised relative to the surface owing to residual stress within it, as shown in Figure 4-15 (a).

The better way is to use transmission light mode to observe it under the optical microscope. Shown in Figure 4-15 (b), a free cantilever looks complete dark due to the large absorption of light by the rough surface of the fabricated grooves.

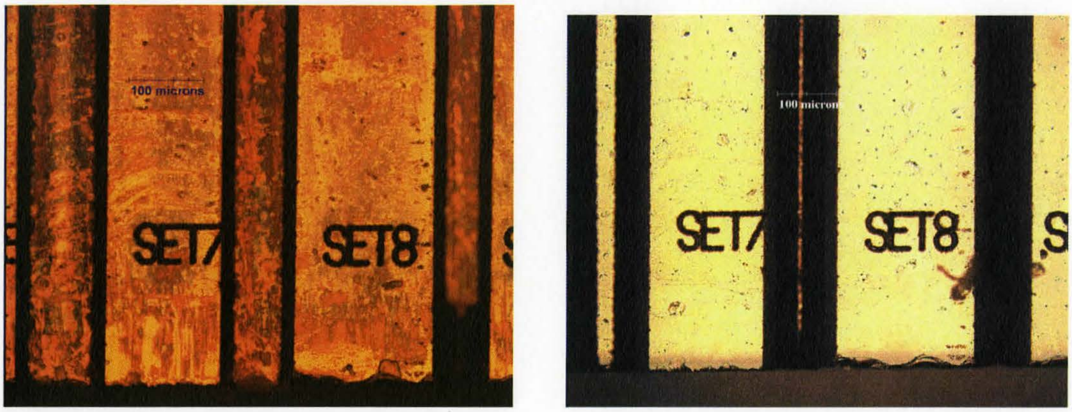

(a) (b)

Figure 4-15: Optical images of cantilevers under (a) normal microscope mode (b) and transmission mode produced by laser machining

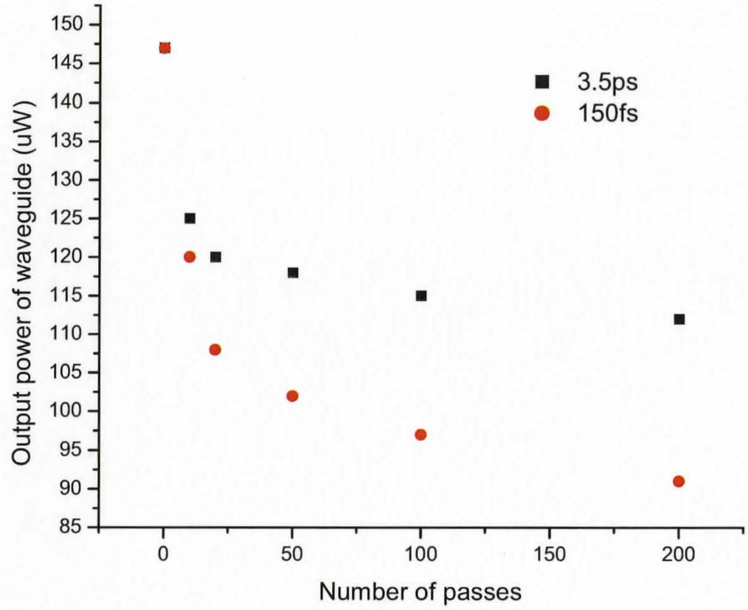

(1)

Figure 4-16: Dependence of waveguide transmission properties on number of passes by laser machining with different pulse durations; Cutting speed: 500μm/s; Laser Power: 3.5mW; Bridge Length: 750μm; Bridge width: 80μm; Tilt angle relative to horizontal plane: 45°

However, fabricating bridges in lithium niobate by laser machining is complicated by the need to minimize any changes to the optical properties of the substrate material near the waveguide.

Figure 4-16 compares the optical transmission performance for two waveguides embedded in the bridges made by femtosecond and picosecond laser respectively. It shows that femtosecond laser machining introduces much more loss into the optical waveguide than machining with picosecond laser pulses. This could be due to the much higher power density of femtosecond laser (more than 20 times higher than that of picosecond laser). Therefore machining with picosecond laser pulses was adopted for the laser machining of structures for MOEMS applications in lithium niobate substrate.

Figure 4-17 shows the decrease of waveguide output power with increase of machining laser power when 3.5 picosecond laser is used for machining process. Apparently, high power introduces more damage to the structure; although it has higher yields as it give deeper depth at the same number of passes and cutting speed.

As mentioned earlier in this chapter, the ripples shown at the bottom of a groove indicate the variance of groove depth and it is related to the cutting speed of machining process. Also, as can be seen in Figure 4-18, the groove made at 200μm/s has much smoother edges than that made at 1000μm/s. The optical test shown in Figure 4-18 also demonstrates that less loss is introduced when slower cutting speed in laser machining process.

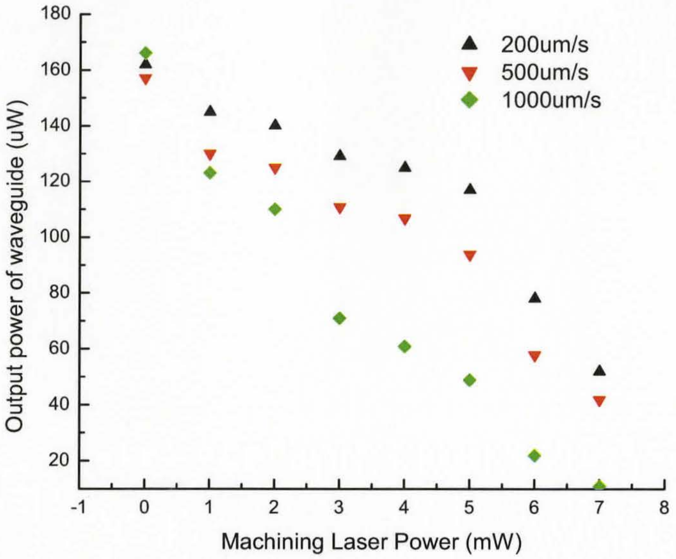

Figure 4-17: Laser pulse duration: 3.5ps; Number of Passes: 100; Bridge Length: 750μm; Bridge width: 80μm; Tilt angle relative to horizontal plane: 45°

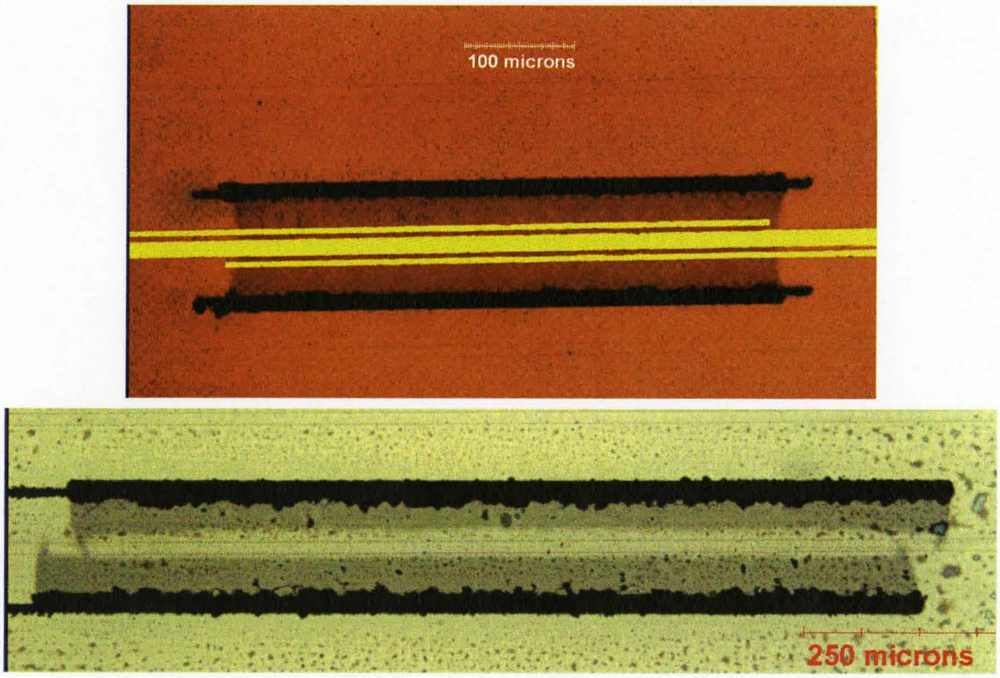

Figure 4-18: Bridges made by 3.5ps laser at 200μm/s and 1000μm/s; Laser power: 3.5mW; number of passes: 100

In summary, in order to produce structures such as bridges and cantilevers by using laser machining in $LiNbO_3$, it is preferred to use picosecond pulses with moderate power and slow cutting speed. A large number of pulses may be required to attain a deep groove depth on the order of 100μm.

Previous work by Paul Driedger indicated that operation at low cutting speed under similar conditions leads the machining process to transit to a modification. This conclusion was confirmed in my work. In the image shown in Figure 4-19, deep modification below the grooves is observed under such conditions. Thus Paul recommends a high cutting speed for laser machining of grooves with high aspect ratio.

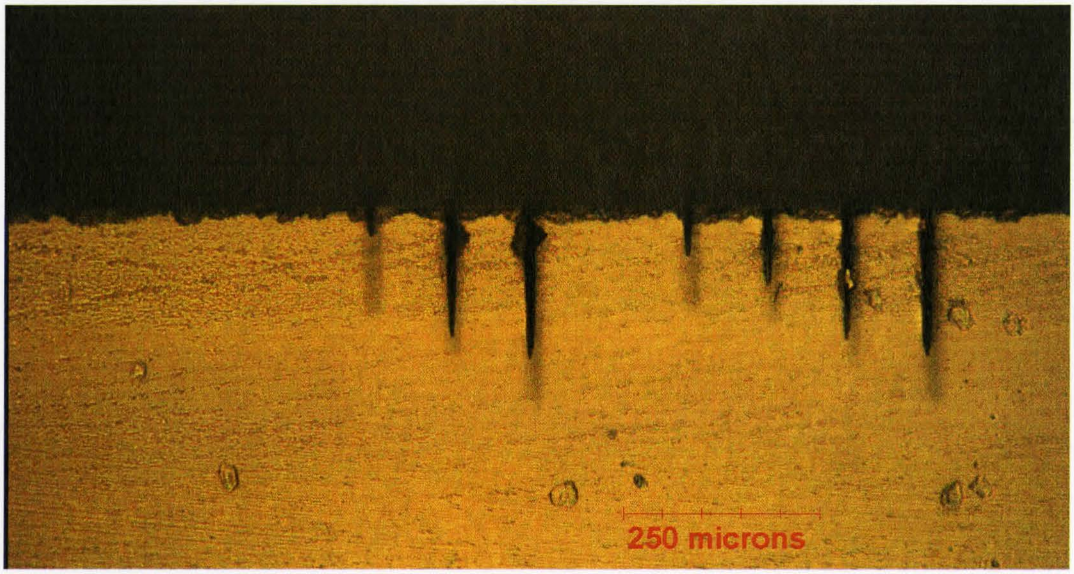

Figure 4-19: End view of grooves made at 350μm/s and 250μm/s showing modification underneath grooves

However, by carrying out a large number of passes the modified material and other debris is removed. This approach also gives the more uniform edge and better performance of the waveguide transmission properties as proved above.

It was found that sometimes the debris was stuck in the bottom of groove and melted again so that the bridge was fixed with the bulk substrate through this melted material. In order to get rid of that, a few of cuttings for each groove were done with the decrease of number of passes for each cutting to make sure the bridge is completely freestanding. Attempt to clean the sample in ultrasonic bath has been made and all of them were broken after the cleaning. While the bridges made by simply machining without re-cutting was still there after the ultrasonic bath, which indicated the "back and forth" cutting during the laser processing ensured that the structure was totally "freestanding". The bridge was then able to vibrate during the ultrasonic cleaning process and consequently led to the break of the freestanding structures.

4.3 Summary

The results of laser machining of lithium niobate in order to fabricate microstructures on it have been presented. Grooves with high aspect ratio were successfully produced with minimal damage to the surrounding material. Grooves width seemed to be determined by laser power other than number of passes and cutting speed. While any grooves depths can be achieved with a high laser power, it is recommended low power, a large number of passes and low cutting speed should be used to minimize the damage to the fabricated structure. Objective lens with magnification of 5 times was utilized and laser was focused 50μm above the surface, which gave the best results for grooves fabrication.

In some cases, there were ripples at the bottom of groove, which means the groove has variations with the depth along the groove length direction. These ripples are not the same phenomenon as LIPSS as the period (~10 μm) is much larger than the typical value for LIPSS. It was found that this problem was alleviated if low cutting speed (500μm/s or less) was used in the laser processing.

Generally for pulse duration less than a few tens of picosecond, laser machining with picosecond laser pulses has the same mechanism as femtosecond laser pulses. However, experiments results show microstructures fabricated by picosecond laser pulses are more robust and mechanically stable than those made by femtosecond laser pulses. Also the picosecond laser introduced less loss into the optical waveguide embedded in the fabricated bridges.

In conclusion, picosecond laser pulses with moderate power and slow cutting speed should be adopted to produce microstructures in lithium niobate substrate. A large number of pulses may be required to attain a deep groove depth on the order of 100μm. Repeated cutting of grooves was necessary to achieve freestanding bridges and cantilevers. An effective way to check the fabrication result is to use transmission light mode to observe it under the optical microscope. A free cantilever would look complete dark due to the large absorption of light by the rough surface of the fabricated grooves.

Chapter 5 Lithium Niobate Waveguide Fabrication

5.1 Lithium Niobate Waveguide Fabrication Techniques

Our devices require optical waveguides to be fabricated on $LiNbO_3$ substrates. The waveguide is defined as a region of high refractive index bounded by regions of lower refractive index. The confinement of the light and the spatial distribution of optical energy inside the guiding area depend on the profile of refractive index and the waveguide dimensions.

Fabricating technique	Treatment	Indices change	Profile	Particular Characteristics
Ti indiffusion	~1000°C for Several hours	Δn_e~0.03 Δn_o ~0.01	Gaussian ~4μm	Electro-optically active; Low optical damage threshold
Proton exchange	200°C exchange in benzoic acid +400°C annealing	Δn_e~0.1 Δn_o ~-0.04	Steplike (before annealing) or Gaussian	Can not be used for Y-cut $LiNbO_3$ substrate; Only support either TE mode or TM mode
Ion implantation He^+ or H^+	~ 2 MeV ~10^{16}ions/cm^2	Δn_e~-0.06 Δn_o~- 0.04	Optical barrier ~5 μm	Decrease of index leads to optical barrier waveguide; Same nonlinear coefficients as in bulk material
ultrafast laser modification 775nm,150fs [14]	circular Polarization Writing velocity: 50μm/s	~6×10^{-4}	Steplike ~15μm	Ability to fabricate complex photonic devices in $LiNbO_3$; Simpler fabrication process than the traditional techniques

Table 5-1 Main characteristics of lithium niobate waveguide fabrication techniques [1]

The general purpose of the waveguide fabrication processes is to produce waveguides with single mode operation at the desired wavelength and low loss. The single mode requirement is determined by dimensions of the waveguides, while the low-loss demand is related with aspects including waveguide structure, surface roughness and boundary layers. The fabrication processes owe much to standard integrated circuits manufacturing techniques. Most waveguides in $LiNbO_3$ crystal are produced by the three conventional techniques - Ti-indiffusion, proton exchange and ion implantation. Focused femotsecond laser is also demonstrated to have the ability to produce waveguide structures in $LiNbO_3$ crystal. The main characteristics of those techniques are summarized in Table 5-1 [1].

The waveguides used in this research were produced using Ti-indiffusion approach. This technique offers the advantage that the waveguide parameters including number of the modes, waveguide width, depth and peak index change can be separately controlled by different fabrication parameters. The fabrication parameters can be set properly to make single-mode waveguides at particular wavelength. Besides the straightforward fabrication process, the Ti-indiffuesd $LiNbO_3$ waveguides are electro-optically active with excellent optical confinement and low transmission loss. These attractive properties have led to the wide use of $Ti{:}LiNbO_3$ waveguide structures in integrated optics.

5.2 Ti-indiffusion Fabrication Theory

Ti-indiffusion technique was first developed by Schmidt and Kaminow in 1974 [15]. It is the most conventional technique for fabricating optical waveguide on $LiNbO_3$ substrate. The diffusion of titanium into $LiNbO_3$ substrates increases the refractive index proportional to the titanium concentration and thus leads to high quality waveguide structure. Ti ions have high activation energy for diffusion and also have high solubility in $LiNbO_3$ at the temperature range from 950 to 1100°C. Titanium has been proved to yield the best result out of a range of different metal indiffusants.

In the Ti-diffusion fabrication process, the photoelastic effect caused by Ti induced strain is a significant contribution to the refractive index change. When the titanium atoms diffuse into the $LiNbO_3$ substrate, they replace the Ni ions in $LiNbO_3$ crystal instead of sitting on the vacancies or defects. The atoms substitution leads to a lattice contraction in the diffused layer, which produces the index change by photoelastic effect. The change of spontaneous polarization in the crystal due to Ti indiffusion also contributes to the refractive index change.

A diffusion model is established from a simplified viewpoint. Assuming that the diffusion time is long enough for the Ti film to completely diffuse into the $LiNbO_3$ substrate, the relative titanium concentration profile as a function of depth y in the crystal should approach the Gaussian function [16]:

$$C(y) = \frac{2a\tau}{\sqrt{\pi}d}\exp[-(\frac{y}{d})^2] \qquad \textbf{5-1}$$

where d is the diffusion depth, a is the number of atoms per unit volume in the deposited film of thickness of τ. The diffusion depth d has a dependence on the diffusion time t and diffusivity D:

$$d = 2(Dt)^{1/2} \qquad \textbf{5-2}$$

where $D = D_0 \exp(-T_0 / T)$, D_0 =2.5×10^{-4} cm^2/s and T_0 =2.5×10^4 K for congruent $LiNbO_3$ composition (48.6mole% of Li_2O).

According to the model, the waveguide depth d (the diffusion depth) depends upon the diffusion time t and the diffusion temperature T. More importantly, the peak substrate index change Δn is determined by the deposited Ti film thickness τ at the fixed diffusion temperature T and time t. Due to lateral diffusion, the peak Ti concentration for strip waveguides also depends on the Ti strip width but to a less extent. The waveguide width is determined by the photolithography step plus the lateral diffusion. Due to the lateral spreading of indiffusant, the guiding region of Ti diffused waveguide is not rectangular. This may improve the coupling efficiency when the fabricated waveguide is coupled with a fiber and therefore reduce loss arising from the mismatch of the shape of the fiber and waveguide electrical fields.

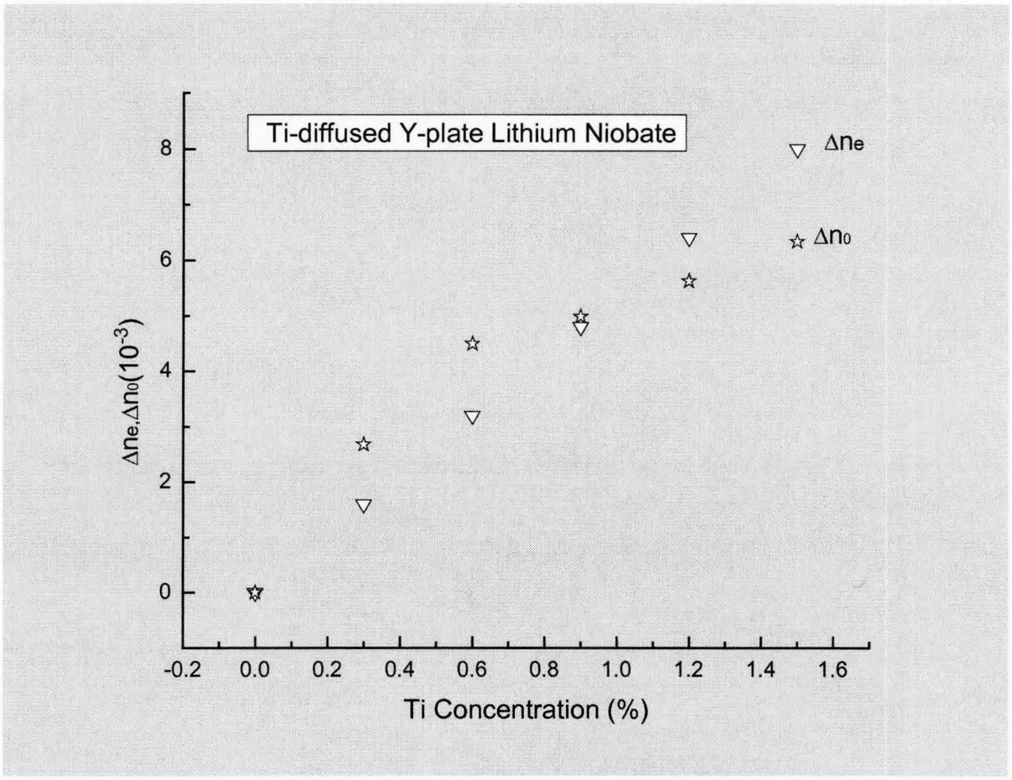

Figure 5-1 Refractive indices changes as a function of Ti concentration at λ=0.63μm [17]

The extraordinary index n_e of fabricated waveguide depends linearly on the Ti concentration, while the ordinary index n_o increases with Ti concentration for small values, and then tends to be saturate when Ti concentration gets large as indicated by Figure 5-1 [17]. Hence, the Ti-indiffusion process usually provides a larger index change for the extraordinary light than that of the ordinary light.

Figure 5-2 shows the diffusion profiles of titanium in $LiNbO_3$ optical waveguides for different diffusion temperature [17]. The waveguides are made in Y-cut $LiNbO_3$ substrates by diffusing Ti film with a thickness of 50nm. The figure indicates that the experimental results match well with the theoretical model. The diffusion profiles are Gaussian distributions with diffusion depth of a few microns. The diffusion depth increases and the maximum Ti concentration decrease with an increase in diffusion temperature.

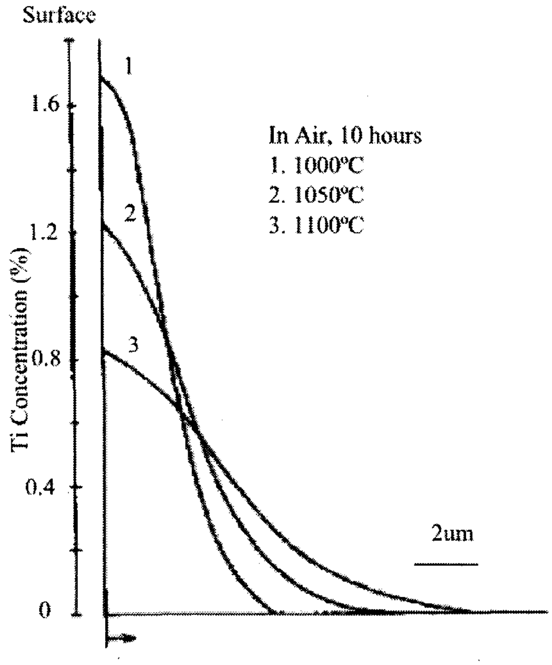

Figure 5-2 Diffusion profiles of Ti in $LiNbO_3$ substrate for different diffusion temperatures [17]

5.3 Lithium Niobate MEMS Device Fabrication Process

This section discusses the mask design and fabrication of lithium niobate waveguides and electrodes for driving purpose. The fabrication process of this device is a multistage process. First the lithium niobate waveguides with low loss are produced. Then silicon dioxide is deposited on top of the whole surface of substrate to eliminate the loss due to direct contact of metal electrodes with waveguides. The third step is to deposit the electrodes by using lift-off technique for actuation purpose. Finally the end facets of the substrate are polished for fiber coupling. A discussion of these processes follows.

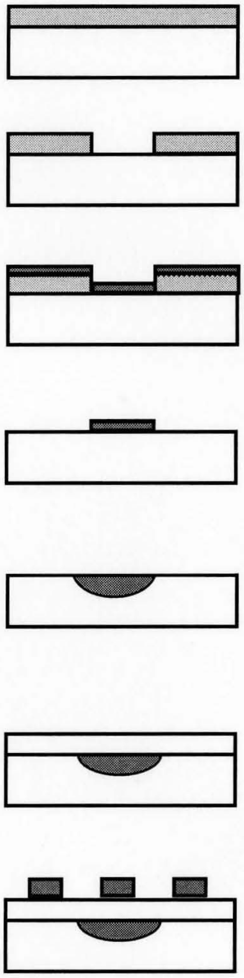

1. $LiNbO_3$ substrate was cleaned and spun with photoresist.

2. A window corresponding to the waveguide pattern was left in the photoresist by photolithographic patterning

3. The Ti film was deposited over the entire crystal. The film thickness will determine the peak refractive index change caused by the diffusion process.

4. Ti film with desired waveguide pattern was formed on the substrate by lift-off technique.

5. Thermal indiffusion of the Ti strip

6. Deposition of 0.3um SiO_2 buffer layer

7. Ti-Pt-Au electrodes deposition on the surface of substrate

Figure 5-3 Lithium Niobate waveguide fabrication process in Z cut substrate by Ti-indiffusion technique; Waveguide length direction is along Y axis of crystal

A simplified description of the waveguide fabrication process by Ti-indiffusion technique is shown in Figure 5-3. At the beginning, the $LiNbO_3$ substrate was carefully examined.

The purpose was to exclude the substrates with excessive defects or internal strain [18]. After careful ultrasonic bath cleaning, photolithography technique was utilized in the process to transfer the desired waveguide pattern onto the substrate. A light sensitive photoresist (S1808) was first spun on the wafer and formed a thin layer on the surface. After baking, the wafer was then selectively exposed by shining light source through a designed mask with the waveguide pattern information. Upon developing the exposed photoresist was removed and a window corresponding to the waveguide pattern was formed in the photoresist.

Titanium with a thickness of 70nm was then deposited on the substrate by using the metallization technique. The Ti deposition rate was set to be 0.3nm/sec because the titanium film thickness and uniformity have to be determined accurately to ensure the desired index change in the resultant waveguide region [19]. The crystal was then placed in a photoresist solvent, which removes the photoresist and the unwanted titanium, leaving the desired strip of titanium.

After the removal of unwanted titanium, the wafer was placed in a diffusion furnace for diffusion at temperature of 1000°C for 8 hours and then allowed to cool. The upper temperature limit was determined to be below the Curie temperature (about 1125 °C) to avoid the needs of repoling after diffusion [20]. During the diffusion process, the titanium diffused into the surface of the material. Sufficiently long diffusion time was needed to ensure all the metal enters into the substrate. If the diffusion is stopped before all the metal enters the crystal, an oxide residue forms on the surface. This could be removed by polishing the surface, but this action is inappropriate for device fabrication because it removes the waveguide trace used to align the electrodes for electro-optic operation.

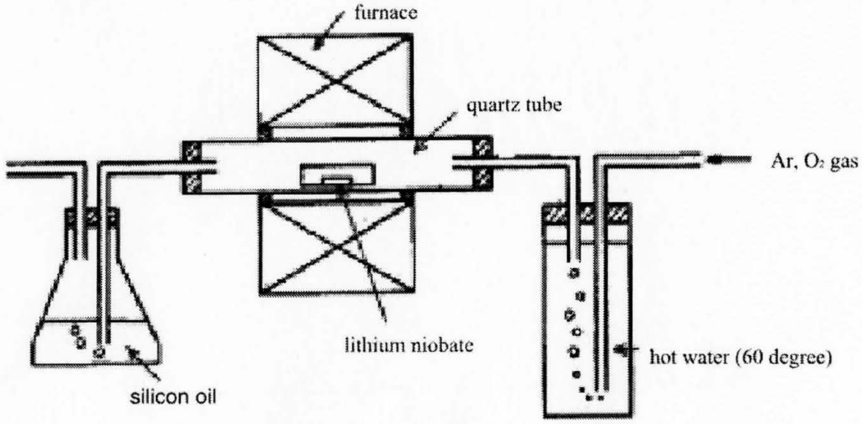

Figure 5-4: Setup for Ti-indiffusion process in the LiNbO$_3$ substrate [19]

Under most processing conditions the diffusion of titanium in a strip was accompanied by an out-diffusion of lithium oxide. This out-diffusion occurred over the whole surface and created a planar guide for extraordinary polarization. Consequently, the extraordinary light can not be well confined in the Ti-indiffused waveguide. This problem could be solved by carrying out the Ti-indiffusion in a controlled atmosphere within the furnace. Our approach was to pass moistened oxygen through the furnace to suppress the out-diffusion, shown in Figure 5-4. It is believed that the presence of excess hydrogen reduces the lithium mobility. This method works reliably and has the advantage of reducing photorefractive effect as well.

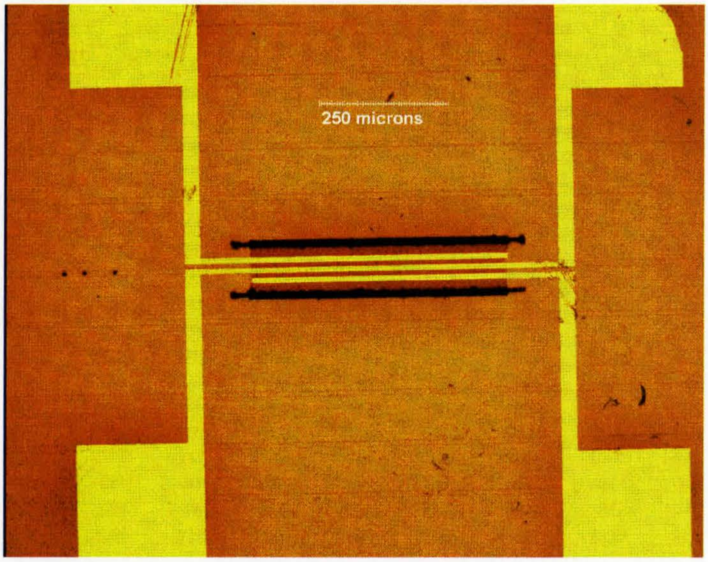

Figure 5-5: Optical image of lithium niobate MEMS device; Bridge length: 500µm; Bridge width: 80µm

After the fabrication of waveguides in lithium niobate, a SiO_2 film with the thickness of 0.3µm was deposited by CVD technique as a buffer layer. Then photolithography process was used to produce the Ti-Pt-Au electrodes in a similar way as the Ti waveguides stripes. The thickness of those three layers was 30 nm, 30 nm, and 300nm, respectively. The next step was to polish both ends of the facets for later optical coupling experiments.

Finally, picosecond laser pulses were employed to produce a bridge on the device so that part of the waveguide is movable under electrical field driving. As discussed before, there are several factors that affect the optical wave transmission in the waveguide. These factors include indices changes due to photoelastic effect and optical length change, electro-optic effect caused by applying external field. This way the optical transmission properties could be controlled by external electrical signal. Figure 5-5 shows the optical image of the fabricated lithium niobate MEMS device. The bridge was produced with 3.5-picosecond laser at 3.5mW, 200μm/s and 100 passes over the grooves. The insertion loss after laser machining is 7.0dB. The next chapter will present the results of waveguide optical transmission properties and the investigation of the resonance frequency of our device.

Chapter 6 Lithium Niobate MEMS Device Characterization

This chapter presents the characterization of lithium niobate MEMS device. Silicon has been used as substrate for most MEMS devices through modern semiconductor fabrication technologies. Lithium niobate has interesting properties like piezoelectric effect, electro-optic effect, photorefractive effect and has great potential for applications in MEMS field.

Through investigations, picosecond laser has been proved to be a viable method to produce lithium niobate microstructures and a bridge with waveguide embedded in it has been successfully fabricated on lithium niobate substrate. After the laser machining, modern semiconductor fabrication technology including PECVD, photolithography and metallization are used to place electrodes on top of the bridge for driving purpose. By applying voltage onto the structure, the bridge is expected to vibrate at the frequency with which the voltage signal is applied. Section 6.1 discusses the Fabry Perot effect in the waveguide transmission. In section 6.2 different kinds of optical loss for the waveguide are investigated. Section 6.2 presents the results of optical and electric tests of our device in order to find the resonance frequency of bridge structure. In the end the summary is given.

6.1 Fabry-Perot Effect

An optical waveguide with two polished end faces can be regarded as a Fabry-Perot resonant cavity. When inputting a laser source from one end of the waveguide, light propagates through the waveguide and reflects at both facets. The amount of reflection is determined by the refractive indices of the waveguide and the external media. As the waves pass the waveguide path back and forth, the waveguide behave as a Fabry-Perot cavity, and the optical intensity of the transmitted light is given by the following Equation 6-1.

$$\frac{I_t}{I_0}=\frac{(1-R)^2 e^{-\partial L}}{(1-Re^{-\partial L})^2+4Re^{-\partial L}\sin^2(\phi/2)} \qquad \textbf{6-1}$$

where R is reflectivity of the facet, L is the waveguide length, ∂ is the loss coefficient, and ϕ is the phase change between successive waves in the resonant cavity. A maximum of intensity can be achieved when $\phi = 2n\pi$, and a minimum value can be achieved when $\phi = (2n+1)\pi$, where $n = 0,1,2,3,...$

According to Equation 6-1, the transfer function is periodic when the phase ϕ passes through multiples of 2π. Therefore the Fabry-Perot cavity is swept through cycles of 2π by either changing the length of the waveguide or the wavelength of the input light source. In our project, a laser with tunable wavelength (ILX Lightwave, 7900B System) was used demonstrate this effect. The schematic of experimental setup is shown in Figure 6-1.

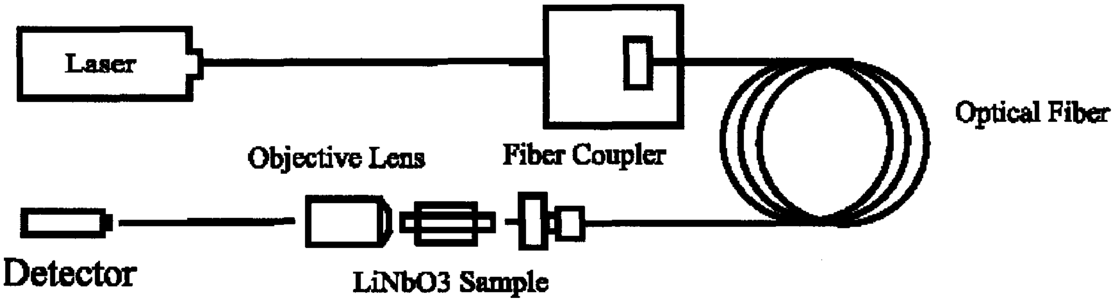

Figure 6-1: Schematic of experimental setup utilized to characterize optical transmission properties of lithium niobate waveguides

The scanning result of the waveguide cavity is shown in Figure 6-2. Equation 6-2 describes the phase of traveling wave in waveguide.

$$\phi = \frac{2\pi n x}{\lambda} \qquad \textbf{6-2}$$

Therefore the change of phase shift can be calculated by Equation 6-3.

$$d\phi = \frac{2\pi n \bullet 2L}{-\lambda^2} d\lambda \qquad \textbf{6-3}$$

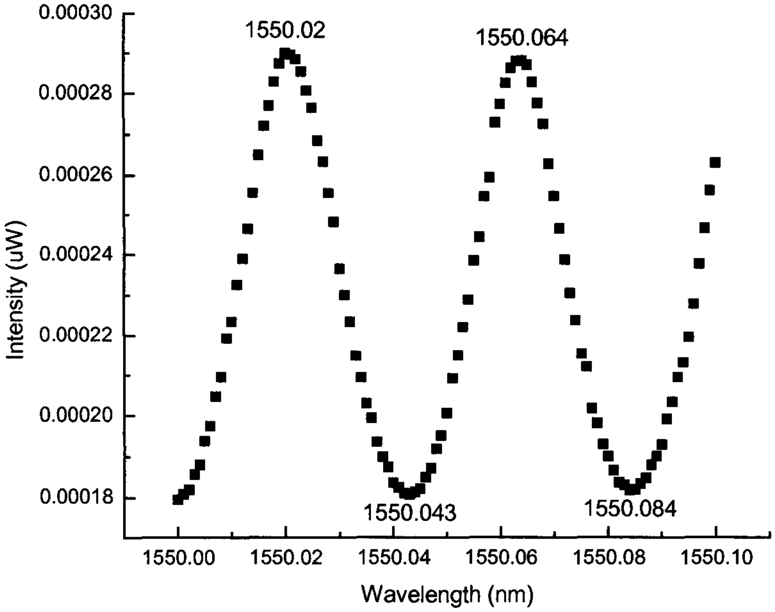

Figure 6-2: Fabry-Perot scanning of lithium niobate waveguide

According to Figure 6-2, a phase shift of π corresponds to a wavelength change from 1550.02nm to 1550.043nm. We can then calculate the waveguide length by Equation 6-4.

$$L = \frac{-\lambda^2 \bullet d\phi}{4n\pi \bullet d\lambda} = \frac{(1550.02\times 10^{-9})^2 \bullet \pi}{4 \bullet 2.2 \bullet \pi \bullet (1550.02-1550.043)10^{-9}} = 0.012\,(\text{Meter}) \qquad \textbf{6-4}$$

This value fits exactly with the real value of sample length. Also through Fabry-Perot effect, transmission loss of waveguide can be determined. More importantly, the optical test of our device relies on this effect, as discussed later in this chapter.

6.2 Loss of Lithium Niobate Waveguide

The insertion loss of waveguide includes coupling loss and propagation loss in our device. The coupling loss consists of Fresnel reflection loss and mode mismatch loss between the fiber and waveguide modes. The total insertion loss L is determined by the input and output power of the waveguide, as described in Equation 6-5.

$$L = -10(\log_{10}\frac{P_{out}}{P_{in}}) = -10(\log_{10}\frac{205}{650}) = 5.012\text{dB} \qquad \textbf{6-5}$$

Equation 6-6 gives the power reflectance at normal incidence for each facet of the waveguide.

$$R = (\frac{n_1 - n_2}{n_1 + n_2})^2 = 0.142 \qquad \textbf{6-6}$$

where n_1 (1.0) and n_2 (2.211) at 1.55 μm) are the refractive indices of the air and lithium niobate substrate, respectively.

6.2.1 Fresnel Loss

The Fresnel reflection loss corresponding to one facet is then given by Equation 6-7.

$$-10(\log_{10}(1-R)) = 0.665 \text{ dB} \qquad \textbf{6-7}$$

Thus the total power loss L_R due to reflection at two facets is 1.330dB.

In the Fabry-Perot scanning of lithium niobate waveguide light transmission, the optical intensity of the transmitted light is described by Equation 6-8.

$$\frac{I_t}{I_0} = \frac{(1-R)^2 e^{-\partial L}}{(1-Re^{-\partial L})^2 + 4Re^{-\partial L}\sin^2(\phi/2)} \qquad \textbf{6-8}$$

where R is reflectivity of the facet, L is the waveguide length, ∂ is the loss coefficient, and ϕ is the phase change between successive waves in the resonant cavity.

The Equation reaches its maximum value when ϕ equals zero, and a minimum value when ϕ equals π, corresponding to Equation 6-9 and 6-10.

$$\frac{I_{\max}}{I_0} = \frac{(1-R)^2 e^{-\partial L}}{(1-Re^{-\partial L})^2} \qquad \textbf{6-9}$$

$$\frac{I_{\min}}{I_0} = \frac{(1-R)^2 e^{-\partial L}}{(1-Re^{-\partial L})^2 + 4Re^{-\partial L}} = \frac{(1-R)^2 e^{-\partial L}}{(1+Re^{-\partial L})^2} \qquad \textbf{6-10}$$

The ratio of the maximum intensity to minimum intensity can then be defined by

Equation 6-11.

$$\frac{I_{\max}}{I_{\min}} = \frac{(1+Re^{-\partial L})^2}{(1-Re^{-\partial L})^2} \qquad \textbf{6-11}$$

Therefore, the value of $e^{-\partial L}$ can be calculated by Equation 6-12.

$$e^{-\partial L} = \frac{(\sqrt{\frac{I_{\max}}{I_{\min}}}-1)}{R(\sqrt{\frac{I_{\max}}{I_{\min}}}+1)} \qquad \textbf{6-12}$$

According to the Figure 6-2, we know the values for $I_{\max}$, $I_{\min}$, R:

$$I_{\max}\text{=0.290 mW},\ I_{\min}\text{=0.181 mW},\ R\text{=0.142} \qquad \textbf{6-13}$$

From Equation 6-12 and 6-13, the value of $e^{-\partial L}$ is determined to be 0.829.

6.2.2 Transmission Loss

The transmission loss L_T is defined by Equation 6-14.

$$L_T = -10(\log_{10}\frac{P_{out}}{P_{in}}) = -10(\log_{10}(e^{-\partial L})) \qquad \textbf{6-14}$$

By substituting the value of $e^{-\partial L}$, the transmission loss L_T is determined to be 0.814dB.

6.2.3 Mode Mismatch Loss

The loss introduced by mode mismatch is strongly dependent on the diffusion conditions of titanium waveguide. The mode mismatch loss L_M due to mode mismatch can be determined to be 2.868 dB by Equation 6-15.

$$L_M = L - L_T - L_R \qquad \textbf{6-15}$$

Now we have characterized all the loss factors of lithium niobate waveguide in our device. The loss due to laser machining is then determined and listed in Table 6-1.

Insertion loss before laser cutting	5.012 dB (205 μW)
Insertion loss after laser machining	6.990 dB ((130 μW)
Loss introduced by laser machining	1.978 dB
Transmission loss	0.814 dB
Reflection loss	1.330 dB
Mode mismatch loss	2.868 dB

Table 6-1: Losses in the waveguide of lithium niobate MEMS device

6.3 Investigation of Bridges Resonance Frequency

The fabricated lithium niobate MEMS device consists of a bridge structure, a waveguide embedded in the bridge and three electrodes on the top, as shown in Figure 6-3.

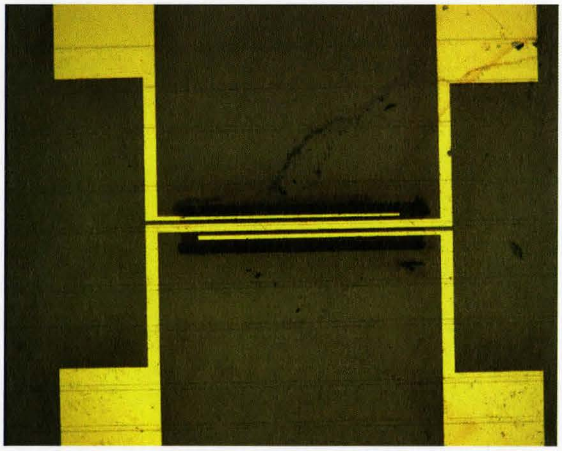

Figure 6-3 Electrodes configuration of the device

6.31 Resonant Frequency Calculation

The Equations used to calculate the fundamental resonant frequency of a bridge with an isosceles triangular cross-section are given by Equations 6-16, 6-17 and 6-18 [21], where E is the elastic modulus, I is the area moment of inertia, g is the acceleration due to gravity, w is the weight per unit length, d is the height of the bridge along vertical direction and b is the side length along lateral direction. $w = \rho \cdot A \cdot g$ and $E = \rho \cdot v_s^2$, where ρ is the mass density, A is the cross-sectional area and $v_s = 6853$ m/s [22] is the speed of sound in the material. The schematic of two bridge vibration modes under sine wave voltage driving are shown in Figure 6-4.

$$f = \frac{22.4}{2\pi}\sqrt{\frac{EIg}{wl^4}} \qquad \textbf{6-16}$$

$I_v = \frac{1}{36}bd^3$ corresponding to vibration frequency f_v along vertical direction **6-17**

$I_l = \frac{1}{48}db^3$ corresponding to vibration frequency f_l along lateral direction **6-18**

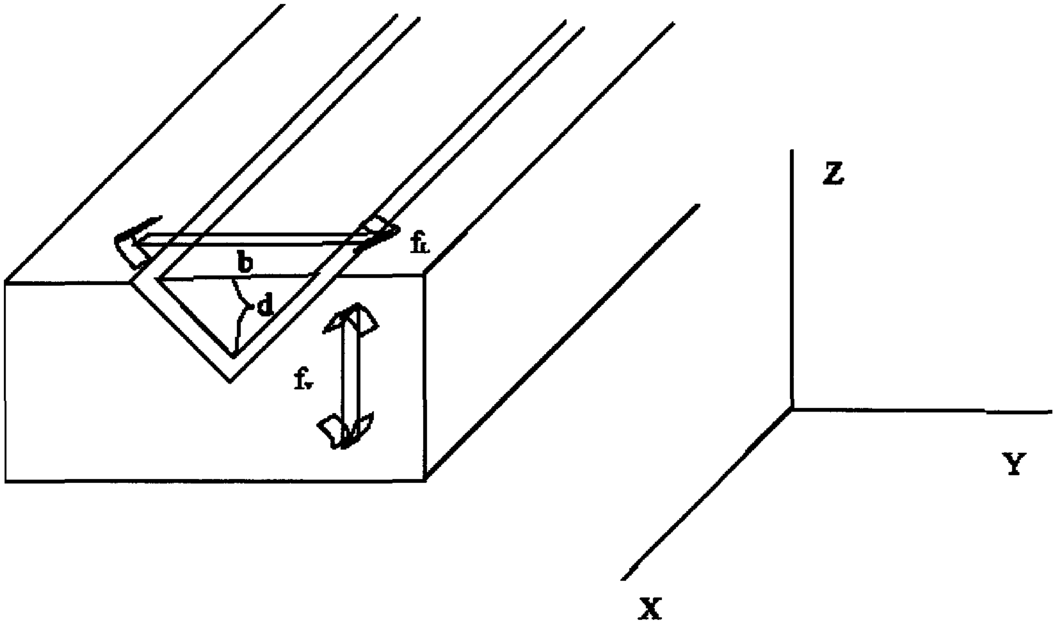

Figure 6-4: Schematic of bridge vibrations under voltage driving

Through calculation, the resonant frequencies along vertical direction f_v and lateral direction f_l for a bridge with b=80 μm d=40 μm and l=560 μm are determined 0.734 MHz and 1.271 MHz, respectively.

6.32 Simulation Results of Bridge Structure Actuation

Figure 6-5 shows the deflection of bridge due to piezoelectric effect when applying sine wave voltage signal with 10 volts amplitude at the resonant frequency of bridge.

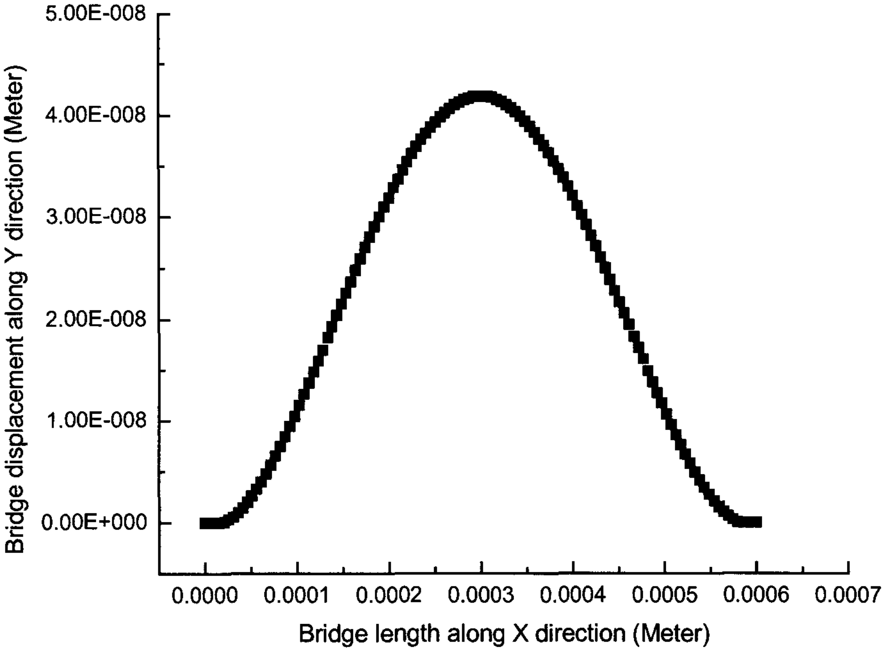

Figure 6-5 Simulation of bridge displacement along Y direction at its resonant frequency

As can be seen from Figure 6-5, the displacement due to length of change is quite small (7.4×10^{-12} m) and thus the contribution to the phase shift is negligible. Next we consider the phase change contribution by the photoelastic effect.

$$\begin{bmatrix} \frac{1}{n_1^2} \\ \frac{1}{n_2^2} \\ \frac{1}{n_3^2} \\ \frac{1}{n_4^2} \\ \frac{1}{n_5^2} \\ \frac{1}{n_6^2} \end{bmatrix} = \begin{bmatrix} p_{11} & p_{12} & p_{13} & p_{14} & 0 & 0 \\ p_{12} & p_{11} & p_{13} & -p_{14} & 0 & 0 \\ p_{31} & p_{31} & p_{33} & 0 & 0 & 0 \\ p_{41} & -p_{41} & 0 & p_{44} & 0 & 0 \\ 0 & 0 & 0 & 0 & p_{44} & p_{41} \\ 0 & 0 & 0 & 0 & p_{14} & (p_{11}-p_{12})/2 \end{bmatrix} \begin{bmatrix} S_1 \\ S_2 \\ S_3 \\ S_4 \\ S_5 \\ S_6 \end{bmatrix} \qquad \textbf{6-19}$$

and we get the change for reflective index along Y direction:

$$\Delta n_y = \frac{1}{2}(p_{12}S_1 + p_{11}S_2 + p_{13}S_3 - p_{14}S_4)n_0^3 \qquad \textbf{6-20}$$

If we assume the strain is uniform along the bridge length and we only consider the TE mode wave, the total phase change of TE mode wave due to photoelastic effect is described by Equation 6-21.

$$\Delta\phi_{\mathrm{TE}} = \frac{2\pi}{\lambda} \bullet \Delta n_y \bullet L \qquad \textbf{6-21}$$

where λ is the wavelength of transmission wave and L is the length of the waveguide.

By using the simulation results, we get $\Delta\phi_{\mathrm{TE}} \approx 6\times10^{-3}$.

Usually we have a power change of 40μW corresponding to a phase change of π for waveguide after laser machining. If we adjust the wavelength of the input laser so that the output power value falls in the middle between the maximum and minimum power values of the scanning spectrum, the power change due to phase change of 6×10^{-3} can be estimated by Equation 6-22.

$$\Delta p = \frac{6\times10^{-3}}{\pi} \times 40\,\mu\mathrm{W} = 0.076\,\mu\mathrm{W} \qquad \textbf{6-22}$$

This amount of power is detectable by the lock-in amplifier we have utilized.

6.32 Optical Characterization of Bridge Structure

There are two methods to determine resonance frequency of the bridge and both of them rely on the piezoelectric effect happening in the structure when an alternating voltage signal is applied onto the structure through electrodes on top of the device.

The first approach is to investigate the waveguide output through a lock-in amplifier with the application of sine wave voltage on the electrodes, as illustrated in Figure 2-3. This produces two main effects. One is electro-optic effect, which is not related with resonant frequency of the device and increases linearly with the voltage on condition that frequency of the sine wave voltage signal is less than gigahertz. When designing the electrodes for driving bridges in our device, the center electrode is determined to have a width of 20μm. While the waveguide width is only around 10μm, which means only a small part of applied field contributes to the electro-optic effect in the waveguide.

The other main effect raised by the application of electrical field is piezoelectric effect. In order to utilize the biggest converse piezoelectric coefficient d_{22}, a bridge structure with the length along X direction in a Z cut substrate has been produced. As shown in Figure 2-3 in Chapter 2, there are three electrodes on top of the bridge. The central electrode is usually grounded and voltage, V, is applied to the other two electrodes. Due to the reverse nature of the directions of the electrical fields on the two sides of the bridge, one half of the bridge expands and while the other half is compressed producing a bimorph bridge. The bridge then vibrates at the frequency with which the voltage signal is applied.

The resultant strain causes a phase path difference ϕ_p through changing the refractive indices of waveguide owing to photoelastic effect. In the meantime, it causes the change of the waveguide path length, and therefore leads to an optical path difference ϕ_l. These phase changes will affect the output of waveguide through Fabry-Perot effect. When signal frequency equals the resonance frequency of the fabricated bridge, the phase change experience the maximum and this can be observed by investigating the output optical signal from the waveguide using a lock-in amplifier.

Sine wave signal is introduced from a function generator (15MHz, Hewlett Packard 33120A) and applied to the electrodes on top of the bridge. The output optical signal from waveguide is detected by an amplified InGaAs detector (PDA10CS, Thorlabs). The detector signal is then received by a RF lock-in amplifier (SR844, Standford Research Systems). Only the signal that has the same frequency with the function generator signal can be detected by the lock-in amplifier.

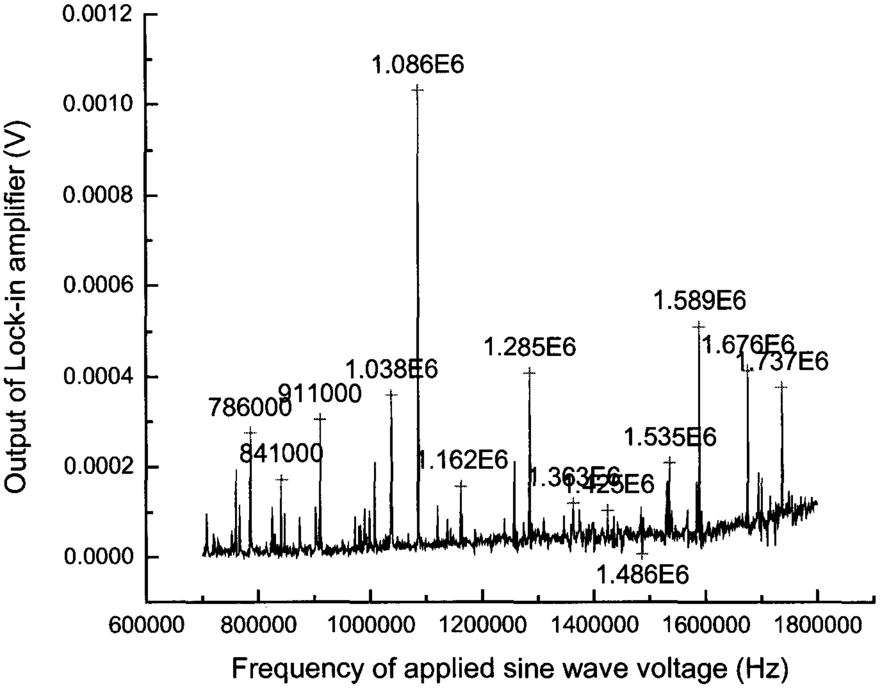

Figure 6-6: Voltage output of lock-in amplifier as a function of input sine wave signal frequency for optical signal test

As can been seen from Figure 6-6, there are more than one peak throughout the frequency scanning range. These additional peaks are probably owing to the bulk material piezoelectric resonance frequencies. In order to prove this assumption, the sample was bonded tightly to a glass slide and the same experiments were performed again. All the main peaks disappeared in the second experiment, which indicated the damping function of glass slide prevented the bulk material from vibrating at their resonance frequencies.

Also, it was found that the experiment results were not replicable, which could be due to a few possible reasons considering the complicated mechanism behind the optical test. The output of the lock-in amplifier is affected by many factors including optical laser source, performance of optical detector and the electrical coupling between the electrodes. Since there are no major peaks and the background curve has many spikes which are not reproducible, the optical test is not applicable for determining the resonance frequencies of our lithium MEMS device.

6.32 Electrical Characterization of Bridge Structure

Another method to determine the resonance frequency of bridge is to apply sine wave voltage signal between the central ground electrode and the electrode on the left side. Due to the piezoelectric effect, voltage is generated between the central ground electrode and the electrode on the right side and received by the lock-in amplifier. When the signal frequency equals the resonance frequency of the bridge structure, a maximum strain is experienced and thus a maximum change of the output from lock-in amplifier is expected.

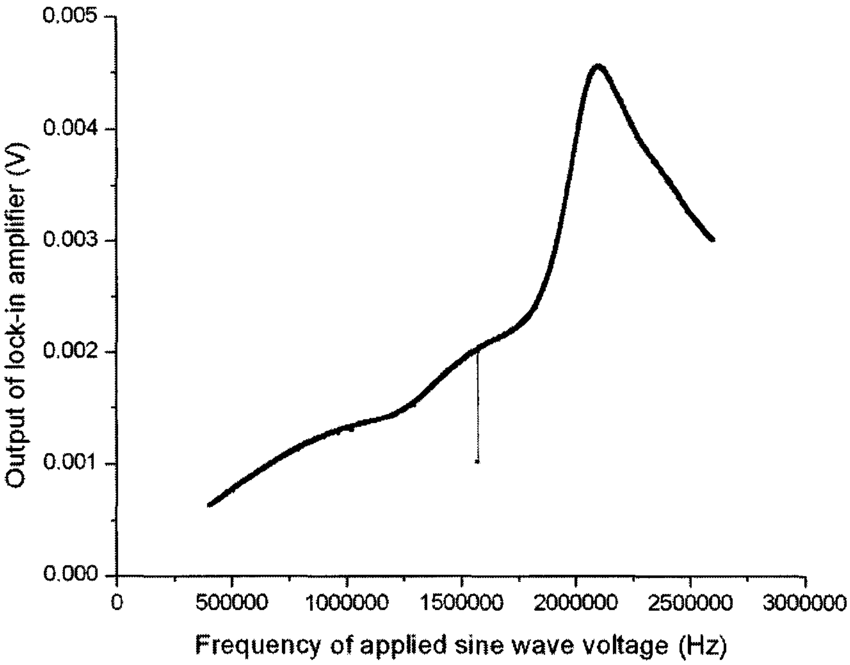

Figure 6-7 Voltage output of lock-in amplifier as a function of input sine wave signal frequency for electrical signal test

This experiment was performed in a small vacuum system in order to increase the Q value of the bridge resonance to make it easier to observe. As show in Figure 6-7, there is a big peak around 1.57 MHz. However, the peak remained the same amplitude and bandwidth when the air went into the system. This indicates this spike could be due to the coupling between the electrodes but not the vibration of the bridge.

The electrical test is reproducible, so it is a better way than optical test to locate the resonance frequency of the device. However, the curve is smooth and no other spikes are found throughout the scanning range.

These two methods rely on piezoelectric effect of the structure, and thus it might not work if the piezoelectricity of the material is damaged. Laser cutting of a freestanding bridge without damaging the surrounding material is a difficult task. The reason why the resonance frequency was not found could be that the laser machining ruined the material properties and consequently destroyed the piezoelectricity of the material.

6.4 Summary

Optical and electrical tests have been performed in order to find the resonant frequency of the bridge. In the optical test, many peaks were found but later we concluded these peaks were due to the bulk material piezoelectric resonance. After fixing the sample to a glass slide, which has a much bigger weight than the sample, no big spikes were found and a background noise with small spikes were obtained. The results for the background and small spikes signal are not reproducible, and therefore the optical test can not be used to determine the resonance frequency of the bridge structure in our device.

Electrical test in a vacuum environment was also carried out and a spike with large amplitude was found. However the characteristic of this spike, including the phase and the amplitude, remained the same after the vacuum condition was removed. This result indicates the spike is not affected by the vacuum condition and thus is not related to the resonance of the bridge.

Although we did not find the real resonance frequency of the device, it is still a good try to make microstructures in lithium niobate substrate. The combination of optical, mechanical and electrical elements will make lithium niobate a great potential for optical MEMS applications.

Chapter 7 Conclusion

Lithium niobate finds a wide range of device applications that exploit its excellent piezoelectric, acousto-optic, electro-optic, pyroelectric and photoelastic properties. Important applications of lithium niobate include directional couplers, surface acoustic wave devices, nonlinear optics devices and intensity modulators.

This thesis presents a viable method to fabricate a MEMS device on lithium niobate substrate in order to explore the potential use of lithium niobate in MEMS field. Characterizations of the device including investigation of waveguide loss and determination of bridge resonance frequency have been undertaken.

Instead of using femotosecond laser pulses, picosecond laser pulses were chosen to produce bridges on lithium niobate substrate. This was based on the stability of the fabricated structure and the introduced loss to the embedded waveguide. Picosecond laser machining shares the same ablation mechanism as femotosecond laser but has much less power density and therefore produces less damage to the surrounding material.

Fabrication of grooves with high aspect ratio was first attempted and the groove edges were clean without much debris around. The groove width is more determined by the laser pulse energy rather than the cutting speed and number of passes. As our goal is to produce high aseptic ratio grooves, low power was therefore adopted for laser machining. This urged us to find a way to produce deep grooves with low laser power.

In some machining conditions, there were ripples at the bottom groove under optical microscope, which indicates there are variations of depth along the length. These ripples are not same as LIPSS and can be eliminated if slow cutting speed is used.

Paul found it was not favorable to use low cutting speed as it produced a lot of debris and modifications of material below the grooves were found after the low speed laser cutting. However, all the debris was finally removed when multiple passes of laser cutting was applied. Moreover, it was found that the variation of grooves depth was related to the cutting speed. With a cutting speed of 500μm/s or less, a deep groove with uniform depth could be easily obtained. Therefore, a low cutting speed, a large number passes of the groove and a low laser power was adopted to cut grooves in lithium niobate. Focusing laser beam 50μm below the sample surface with objective lens of 5 times magnification gave the best results of machining.

After the fabrication of waveguides in lithium niobate, a SiO_2 film with a thickness of 0.3μm was deposited by CVD process as a buffer layer to avoid the loss induced by direction contact between electrodes and waveguide region. Ti-Pt-Au electrodes were then deposited on top of waveguide through lift-off technique. Both end facets of the substrate were polished to minimize the coupling loss between the waveguide and input fiber. The final step was to use picosecond laser to produce a bridge on the device. The bridge was successfully fabricated with 3.5-picosecond laser at 3.5mW. Cutting speed of 200μm/s was used and 100 passes were performed over the grooves.

Optical transmission properties of waveguide and resonance frequency of our device were then investigated. The insertion loss before and after laser machining is 5.01dB and 6.99dB respectively.

Optical and electrical tests were performed in order to find the resonant frequency of the bridge. In the optical test, many peaks were presented in the frequency spectrum and these peaks were due to the bulk material piezoelectric resonance. After fixing the sample to a glass slide to damp the vibration of the substrate, these spikes disappeared and only a background noise with small spikes were obtained. Due to the non-replicable nature of the optical test, the resonance frequency of the bridge structure in our device could not be determined through this method.

The electrical test was carried out in a vacuum environment. A spike with large amplitude was found. After removing the vacuum condition, the phase and amplitude of the spike remained the same. This indicates the spike is not affected by the vacuum condition and thus is not related to the resonance of the bridge.

Although our device could not be driven to vibrate at its resonance frequency, there is a great deal of promise making microstructures in lithium niobate substrates. The combination of optical, mechanical and electrical elements will make lithium niobate a great potential material for optical MEMS applications. Future work could involve directly investigating the properties of material surrounding the machining area to see whether the piezoelectricity of the material has been damaged from laser machining. New laser machining process of lithium niobate may need to be studied to avoid this damage to the substrate structure.

Appendix:

Device Fabrication

Fabrication Procedure for Lithium Niobate Waveguides

1. Wafer Cleaning:

Put the sample in a sample holder for cleaning.
Use acetone as the solution and put the sample in ultrasonic machine for 5 minutes.
Repeat the same procedures by using methanol and deionized water respectively.
Take out the wafer and place it perpendicularly on the table and blow it with nitrogen gun.
Soft bake at 65° C for 10 minutes.

2. Photolithography for Ti diffusion

Apply Photoresist S1808 – spin 400 rpm for 30 seconds
Wait 5 minutes in the air
Soft bake at 90° C for 2 minutes
Expose in mask aligner for 4 seconds at 10mW/cm^2
Put it in Toluene for 6 minutes and dry it by using nitrogen gun
Overdevelop for 1.5 minutes in 5:1 deionized water:351 Developer solution
Rinse it in deionized water

3. Ti Metallization

Titanium metallized in the deposition chamber with vacuum of 10^{-8} Torr at an average deposition rate of 0.3nm/sec

4. Lift-off process

Put the wafer in a beaker with acetone solution and allow metal to lift from the surface
After 2 hours, spray acetone on the surface to speed up the lift-off process
Use Q-tip to remove the resident unwanted metal
Put the wafer back in a beaker with methanol solution for half an hour
Clean it in deionized water and dry it

5. Titanium diffusion

Place sample in the furnace on a quartz slide for diffusion
Turn on the furnace and set the temperature to 1000°C
When the temperature reach 600°C, switch on moistened oxygen through the furnace
Turn off the furnace after 8 hours
Turn off the oxygen flow after the furnace temperature reaches 600°C

Take out the sample from the furnace after the furnace reaches room temperature

6. CVD for SiO_2 buffer layer deposition
Wait for the temperature to go up to 300° C
Turn the knob to set mode and set gas to desired flow rate: N_2O: 70; SiH_4: 90
Set pressure controller to 650 mTorr
Set the deposition Time to 4'15", and SiO_2 with the thickness of 300nm is deposited

7. Ti-Pt-Au electrodes lift-off
Follow procedure 2, 3, 4

8. Polishing the end facets
Cut the wafer into small samples (1.2cm × 0.8cm)
Mount the samples to polishing chuck
Polish each end of the samples on 400 grit, 600grit, 6μm, 1μm, and 0.05μm polishing surfaces.
Examine the polish surface under microscope for each step
Clean the samples with acetone, methanol and deionized water in ultrasonic cleaner
Dry the samples with nitrogen gun

References

[1] L. Arizmendi, *Physica Status Solidi A*, **201 (2)**, 253-283 (2004)

[2] R.S. Weis, T.K. Gaylord, *Applied Physics A* **37 (4)** (1985) 191-203

[3] N. Mitsugi, H. Nagata, *The Journal of Vacuum Science and Technology* **16 (4)** (1998) 2245-2251

[4] P. Bunton, M. BinKley, G. Asbury, *Apply Physics A*, **65 (4)**, 411-417 (1997)

[5] Paul Driedger, "Femtosecond laser micromachining of lithium niobate", Master thesis, McMaster University, 2006

[6] J.F.Nye, "*Physical Properties of Crystal*", Oxford Univ. Press, 1957, page248

[7] X. Liu, D. Du, and G. Mourou, *IEEE Journal of Quantum Electronics*, **33 (10)**, 1706-1716 (1997)

[8] D. Du, X. Liu, G. Korn, J. Squier, and G. Mourou, *Applied Physics Letters*, vol. **64 (23)**, pp.3071-3073, 1994

[9] J.M. Liu, *Optics Letters*, **7(5)**, 196-198 (1982)

[10] M. Lawrence, *Reports on Progress in Physics*, **56 (3)**, 363-430 (1993)

[11] J.E.Sipe, J.F. Young, J.S. Preston, H.M. van Driel, *Physical Review B* **27 (2)**, 1141-1145 (1983)

[12] J.F. Young, J.S. Preston, H.M. van Driel, J.E. Sipe, *Physical Review B* **27 (2)**, 1155-1172 (1983)

[13] Z. Guosheng, P.M. Fauchet, A.E. Siegman: *Physical Review B,* **26 (10)** 5366-5381 (1982)

[14] L. Gui, B. Xu, and T.C. Chong, *IEEE Photonics Technology Letters*, **16 (5)** 1337-1339 (2004)

[15] R. V. Schmidt and I. P. Kaminow, *Applied Physics Letter*, **25 (8)**, 458-460 (1974)

[16] P. G. Shewmon, *Diffusion in Solids* (McGraw-Hill, New York, 1963)

[17] M. Minakata, S. Saito, M. Shibata, and S. Miyazawa, *Journal of Applied Physics* **49 (9)**, 4677-4682 (1978)

[18] T. Tamir, *Guided-Wave Optoelectronics* (Springer-Verlag, New York, 1990)

[19] Nishihara H. et. Al., *Optical Integrated Circuits* (Mc-Graw Hill, 1989)

[20] K. Sugii, M. Fukuma, H. Iwasaki, *Journal of Materials Science* **13 (3)**, 523-533 (1978)

[21] W. C. Young, *Roark's Formulas for Stress & Strain* (M-Graw Hill, 1989)

[22] *Properties of Lithium Niobate*, by INSPEC (information service) London ; New York : INSPEC, Institution of Electrical Engineers, c1989.